PHYSICAL REVIEW B **92**, 085138 (2015)

Chiral degeneracies and Fermi-surface Chern numbers in bcc Fe

Daniel Gosálbez-Martínez,[1,2] Ivo Souza,[1,3] and David Vanderbilt[4]
[1]*Centro de Física de Materiales, Universidad del País Vasco, 20018 San Sebastián, Spain*
[2]*Donostia International Physics Center, 20018 San Sebastián, Spain*
[3]*Ikerbasque Foundation, 48013 Bilbao, Spain*
[4]*Department of Physics and Astronomy, Rutgers University, Piscataway, New Jersey 08854-8019, USA*
(Received 28 May 2015; published 21 August 2015)

The degeneracies in the spinor band structure of bcc Fe are studied from first principles. We find numerous isolated band touchings carrying chiral charges of magnitude one (Weyl points) or two (double-Weyl nodes), as well as nonchiral degeneracy loops (nodal rings). Some degeneracies are located on symmetry lines or planes in the Brillouin zone and others at generic low-symmetry points, realizing all possible scenarios consistent with the magnetic point group. We clarify the general theory relating the chiral band touchings to the Chern numbers of the Fermi sheets enclosing them and use this approach to determine the Chern numbers on the Fermi surface of bcc Fe. Although most Fermi sheets enclose Weyl nodes, in almost all cases the net enclosed charge vanishes for symmetry reasons, resulting in a vanishing Chern number. The exceptions are two inversion-symmetric electron pockets along the symmetry line Δ parallel to the magnetization. Each of them surrounds a single Weyl point, leading to Chern numbers of ± 1. These small topological pockets contribute a sizable amount to the nonquantized part of the intrinsic anomalous Hall conductivity, proportional to their reciprocal-space separation. Variation of the Fermi level (or other system parameters) may lead to a touching event between Fermi sheets, accompanied by a transfer of Chern number between them.

DOI: 10.1103/PhysRevB.92.085138 PACS number(s): 75.47.−m, 75.50.Bb, 71.18.+y, 73.43.−f

I. INTRODUCTION

The degeneracies in three-dimensional (3D) band structures that are not lifted by the spin-orbit interaction are receiving increasing attention in connection with topological states of matter. Murakami [1] showed that, in the absence of inversion symmetry (P), a gapless crystalline phase can exist over a finite region of parameter space between a topological insulator and a normal insulator. This *Weyl semimetal* phase is characterized by topologically protected isolated touching points—the Weyl points (WPs)—between valence and conduction bands, and its low-energy excitations are described by a generalized Weyl equation of the form $H(\mathbf{k}) = k_i v_{ij} \sigma_j$, where $\mathbf{k}$ is the wave vector relative to the touching point and $\{\sigma_i\}$ are the three Pauli matrices plus the 2×2 identity matrix. Similar phases were later devised where time-reversal symmetry (T) is broken instead of parity P [2,3].

Weyl semimetals are expected to have interesting transport properties. In particular, the magnetic variety can have a nonzero intrinsic anomalous Hall conductivity (AHC) proportional to the separation in k space between WPs of opposite chirality [4], where the chirality of a WP is $c = \mathrm{sgn}(\det v) = \pm 1$. Like other topological phases, Weyl semimetals display a bulk-boundary correspondence: Pairs of WPs of opposite chirality at the Fermi level E_F lead to metallic "Fermi arc" surface states connecting their projections onto the surface Brillouin zone (BZ) [2,5,6].

Real-world examples of Weyl semimetals have been recently identified. Compounds in the TaAs family were predicted to be P-breaking Weyl semimetals [7,8], and the observation of Fermi-arc surface states using angle-resolved photoemission spectroscopy was reported soon afterwards for both TaAs and NbAs [9–11]. Another promising candidate is BiTeI, which is known to undergo a normal-to-topological transition under pressure and must have a Weyl phase for some interval of pressure [12] even if it has not yet been observed. There has also been recent progress in realizing a related phase that preserves both P and T symmetries, the *Dirac semimetal* [13,14]. Here the bands are everywhere Kramers degenerate, so that a total of four bands meet at the Fermi point.

More generally, isolated band touchings can occur at arbitrary energies in 3D band structures with broken PT symmetry. Under those conditions accidental degeneracies that occur away from symmetry lines and planes have codimension three, which implies that the parameters (k_x, k_y, k_z) provide just enough degrees of freedom to bring a pair of bands together at generic isolated points in the BZ [1]. With some exceptions (see below), isolated degeneracies in a 3D parameter space are robust topological objects, acting as monopole sources and sinks of Berry curvature [15]. This accounts for their remarkable stability, as well as for many of the interesting phenomena associated with them.

Weyl points, defined as linear crossings carrying a topological (chiral) charge ± 1, are not the only type of isolated degeneracy in 3D band structures. Quadratic or cubic crossings carrying a charge of ± 2 or ± 3 are also possible along certain symmetry axes; they can be viewed as several WPs of the same chirality brought together by point-group symmetry [16]. We use the term *point node* (PN) to denote a generic isolated degeneracy and reserve the terms *WP* and *double-Weyl node* for the specific types that we encounter in bcc Fe (triple-Weyl nodes are disallowed in tetragonal ferromagnets, as they can only occur along a sixfold axis).

In addition, it is possible to arrange, via external fine tuning, for isolated band touchings of other types. This can occur, for example, in the context of a normal-to-topological transition in a P-broken, T-invariant system; at the critical parameter values at which pairs of Weyl nodes with opposite chiralities are first created or finally annihilated, there is a quadratic band

touching of zero overall chiral charge [1,17]. Since these are not generic, however, they do not play any further role in our considerations.

In some cases symmetry can glue bands together at a high-symmetry point or along a high-symmetry line. For ferromagnetic crystals with the spin-orbit interaction included in the Hamiltonian, a group-theoretical analysis [18–20] has shown that such degeneracies can be present when the structure is hexagonal (e.g., hcp Co), but not when it is tetragonal. Indeed, we have not encountered this type of degeneracy in our present study of the spinor band structure of bcc Fe.

Finally, the spinor energy bands of a ferromagnet can also remain degenerate along entire loops lying on BZ planes that are invariant under reflection (i.e., mirror planes). We refer to this type of degeneracy as a *line node* or *nodal ring*.

In metals, chiral degeneracies in the band structure may induce nonzero Chern numbers on the Fermi-surface (FS) sheets. This possibility was first considered by Haldane in connection with the FS formulation of the intrinsic AHC [6,21]. Topologically nontrivial Fermi sheets have also been discussed in the context of topological superconductivity [22,23] and of the chiral magnetic effect and related effects in Weyl semimetals [24]. Metals with topological Fermi sheets are sometimes called *topological metals* [6,8], and the ideal Weyl semimetal corresponds to the limiting case in which the topological pockets collapse onto isolated Fermi points (and no additional Fermi sheets are present).

In spite of all these formal developments, little is known about the occurrence of PNs, nodal rings, and especially topologically nontrivial Fermi sheets in everyday real materials. Are they extremely rare, or very common, in the electronic structure of typical T-broken crystals such as ferromagnetic metals? How does their presence affect physical observables associated with the k-space Berry curvature, notably the AHC? A few studies of chiral degeneracies have been conducted recently on model band structures of photonic [25] and ferromagnetic [26] crystals and on *ab initio* band structures of P-broken semiconductors and Weyl semimetals [7,8,27,28]. Otherwise, however, there has been remarkably little discussion in the literature and, in particular, virtually no systematic searches for topological Fermi sheets using first-principles methods.

In this paper, we clarify the formal relations between chiral PNs in the band structure of metals with broken PT symmetry and the Chern numbers of the individual Fermi sheets. Furthermore, we examine in detail the role of chiral PNs and topological Fermi sheets in the intrinsic AHC of T-broken metals. To that effect, we decompose the AHC band-by-band and in terms of Fermi sheets and show how the two decompositions are related by k-space dipole moments of the occupied chiral PNs, which vanish upon summing over all bands. This analysis clarifies further (see also Ref. [29]) why the presence of chiral degeneracies below E_F is not an impediment to a purely FS formulation of the nonquantized AHC, contrary to a recent claim [26]. We also elucidate the relation between two alternative FS formulations of the AHC, one in terms of Berry curvatures and Berry phases [21], the other in terms of Berry phases only [30].

In order to see how these ideas play out in real materials, we decided to give a complete census of all the degeneracies and their topological charges and then use that information to determine the Fermi-sheet Chern numbers in one or more simple ferromagnetic metals. Taking bcc Fe as our first test case, we found to our surprise that chiral PNs are astonishingly ubiquitous in the band structure. For example, we find 90 of them between bands six and seven alone. In the present work we therefore chose to concentrate entirely on bcc Fe as a paradigmatic system to illustrate the concepts and search strategies. Interestingly, we find that bcc Fe is, at least within our density-functional theory calculation using a generalized-gradient approximation (see Sec. V), a T-broken topological metal in the sense of Haldane [6]. That is, a pair of Fermi pockets have equal and opposite nonzero Chern numbers and contribute significantly to the AHC.

The complex band structure of bcc Fe proves to be a flexible arena for exploring the physics of topological metals beyond simple Weyl semimetals. For example, we demonstrate that Chern numbers can be transferred between Fermi sheets by varying the Fermi level or an external parameter such as the magnetization direction. Topological transitions of this kind have been discussed previously in the literature for model Hamiltonians [31,32], but the detailed mechanisms have not been investigated for real metals. Even though the touching events leading to the Chern-number exchange occur locally between sheets on adjacent bands, in bcc Fe we find that these events are often concerted, e.g., such that the Chern number gets transferred between two sheets on the *same* band via an intermediary "passive" sheet in the band below.

We emphasize from the outset the crucial role played by the spin-orbit interaction in the present study, where the Bloch states are treated as spinors. Iron is a mostly collinear ferromagnet with fairly weak spin-orbit coupling (SOC), but for our purposes "weak SOC" is completely different from "zero SOC," as it changes qualitatively the nodal structure of the bands and the connectivity of the FS [33–35]. Moreover, SOC induces a k-space Berry curvature on the Bloch states by transmitting the breaking of time reversal from the spins to the orbital degrees of freedom. Without SOC, the up-spin (minority) and down-spin (majority) bands are decoupled, and in each spin channel the spatial wave functions are T invariant (in addition to being P invariant). Without SOC, the Berry curvature vanishes identically in iron as a result of this effective PT symmetry, and generic like-spin degeneracies have codimension two, not three; i.e., they are line nodes instead of isolated PNs. For opposite-spin crossings one gets entire nodal surfaces on which $E_{n\uparrow}(\mathbf{k}) = E_{m\downarrow}(\mathbf{k})$. However, even a weak SOC gaps these curves and surfaces almost everywhere, reducing the locus of degeneracies to a collection of discrete points (and occasionally, on mirror planes, a few loops). The weakness of the spin-orbit interaction makes for a challenging computational problem, since true band crossings coexist with, and must be distinguished from, minute spin-orbit-induced avoided crossings.

The paper is organized as follows. Some definitions, notation, and basic relations are given in Sec. II. In Sec. III we work out the relations that allow the determination of the Chern numbers of the Fermi sheets from a knowledge of the population of chiral degeneracies in the energy bands. In Sec. IV we consider the role played by chiral PNs in the theory of the intrinsic AHC, particularly in relation to FS-based

formulations. In Sec. V we describe the electronic structure methods that were used in our calculations on bcc Fe. The numerical results are presented and discussed in Sec. VI, and we conclude in Sec. VII with a summary.

II. DEFINITIONS AND BASIC RELATIONS

A. Berryology

The k-space Berry connection of band n

$$\mathbf{A}_n(\mathbf{k}) = i\langle u_{n\mathbf{k}}|\nabla_{\mathbf{k}} u_{n\mathbf{k}}\rangle \tag{1}$$

is defined in terms of the cell-periodic Bloch states $|u_{n\mathbf{k}}\rangle = e^{-i\mathbf{k}\cdot\mathbf{r}}|\psi_{n\mathbf{k}}\rangle$. A geometric phase (Berry phase) can be associated with a closed path $\mathcal{C}$ in k space by taking the circuit integral of the connection,

$$\varphi_n(\mathcal{C}) = \oint_{\mathcal{C}} d\mathbf{k}\cdot\mathbf{A}_n(\mathbf{k}). \tag{2}$$

The Berry curvature is the curl of the connection,

$$\mathbf{\Omega}_n(\mathbf{k}) = \nabla_{\mathbf{k}}\times\mathbf{A}_n(\mathbf{k}), \tag{3}$$

so that, according to Stokes' theorem, $\hat{\mathbf{n}}\cdot\mathbf{\Omega}_n(\mathbf{k})$ has the interpretation of a Berry phase per unit area for a small planar loop with unit surface normal $\hat{\mathbf{n}}$. The Berry connection is gauge dependent, meaning that its value at $\mathbf{k}$ can be changed continuously by modifying the phase choice for the Bloch eigenstates around $\mathbf{k}$. The Berry phase is gauge invariant apart from a 2π indeterminacy, and the Berry curvature is fully gauge invariant. Like the energy bands $E_n(\mathbf{k})$, the Berry curvature has the periodicity of the reciprocal lattice, $\mathbf{\Omega}_n(\mathbf{k}+\mathbf{G}) = \mathbf{\Omega}_n(\mathbf{k})$.

Chern's theorem. The Berry-curvature flux through a closed oriented surface $\mathcal{S}$ in k space is equal to $2\pi C_n(\mathcal{S})$, where $C_n(\mathcal{S})$ is an integer known as the Chern number:

$$C_n(\mathcal{S}) = \frac{1}{2\pi}\oint_{\mathcal{S}} dS\,\hat{\mathbf{n}}\cdot\mathbf{\Omega}_n(\mathbf{k}). \tag{4}$$

This statement is valid provided that band n remains nondegenerate over the entire surface.

A 2D BZ is effectively a closed surface by virtue of the periodicity of k space, so that Chern's theorem applies, and the same is true for a 2D section of a 3D BZ cut along reciprocal-lattice vectors. Consider a cubic lattice (simple cubic, bcc, or fcc): The Chern number of band n on a BZ slice taken at fixed k_z is

$$C_n(k_z) = \frac{1}{2\pi}\int_{\text{slice}} d^2k\,\Omega_{n,z}(\mathbf{k}), \tag{5}$$

where the integral is over a primitive cell on the (k_x,k_y) plane at fixed k_z. Viewed as a function of k_z, the slice Chern number $C_n(k_z)$ is a piecewise constant integer function. It can only change at critical k_z values, where band n comes in contact with a contiguous band $n\pm1$ at isolated points; when that happens, $C_{n\pm1}(k_z)$ changes by a compensating amount, and the process can be viewed as an exchange of an integer amount of Chern number between the two bands [36]. The periodicity condition

$$C_n(k_z + 2\pi/a) = C_n(k_z) \tag{6}$$

(a is the cubic lattice constant) implies that the smallest nonzero number of integer steps over one period is two.

Another example of a closed surface is an isolated Fermi sheet. Even though some Fermi sheets may look open because of being cut at the BZ boundary, they are, in fact, closed manifolds in the topological sense, when equivalence under reciprocal-lattice translations is factored in (as, for example, for the well-known shape of the FS in Cu). Thus, Chern's theorem applies and isolated Fermi sheets always have a topological index [6,21]. (The possibility that two sheets touch, either as a result of fine tuning or because of symmetry, should be kept in mind.)

One can also associate a Chern number with a composite group of bands over a closed surface. We consider the group formed by the n lowest bands and define, for a BZ slice,

$$\widetilde{C}_n(k_z) = \sum_{l=1}^{n} C_l(k_z). \tag{7}$$

The index $\widetilde{C}_n(k_z)$ inherits the properties already discussed for $C_n(k_z)$, but it only reacts to touching events between the uppermost band n in the group and band $n+1$ above and is instead oblivious to band crossings within the group.

A related quantity of interest is the Berry flux through a bounded oriented surface $\mathcal{S}$ in the BZ,

$$\phi_n(\mathcal{S}) = \int_{\mathcal{S}} dS\,\hat{\mathbf{n}}\cdot\mathbf{\Omega}_n(\mathbf{k}). \tag{8}$$

For example, $\mathcal{S}$ could be a patch on a BZ slice, threaded by a nonquantized flux ϕ_n, or an entire slice, now viewed as an open rectangle rather than a closed 2-torus (quantized flux $\phi_n = 2\pi C_n$). If a smooth gauge is chosen for the Bloch states on the boundary $\mathcal{C}$ of $\mathcal{S}$, then the Berry phase computed on $\mathcal{C}$ is equal, modulo 2π, to the Berry flux through $\mathcal{S}$ [37],

$$\varphi_n(\mathcal{C}) = \phi_n(\mathcal{S}) \bmod 2\pi. \tag{9}$$

B. Isolated band touchings (point nodes)

We denote by $W_{n\alpha}$ the αth PN between bands n and $n+1$, located at $(\mathbf{k}_{n\alpha}, E_{n\alpha})$ and with integer chiral charge $\chi_{n\alpha}$. It follows from Eq. (3) that $\nabla\cdot\mathbf{\Omega}_n = 0$ everywhere except at the PNs, which act as monopole sources of Berry flux. Our sign convention for χ is that the PN acts as a source of $2\pi\chi$ Berry flux in the lower band and as a sink of $2\pi\chi$ Berry flux in the upper band. Thus,

$$\nabla\cdot\mathbf{\Omega}_n(\mathbf{k}) = 2\pi\sum_{\alpha}\chi_{n\alpha}\delta^3(\mathbf{k}-\mathbf{k}_{n\alpha}) - 2\pi\sum_{\alpha}\chi_{n-1,\alpha}\delta^3(\mathbf{k}-\mathbf{k}_{n-1,\alpha}). \tag{10}$$

For any connected subvolume $\mathcal{V}$ of the BZ with boundary $\mathcal{S}$, the divergence theorem applied to band n gives

$$\oint_{\mathcal{S}} dS\hat{\mathbf{n}}\cdot\mathbf{\Omega}_n = \int_{\mathcal{V}} dV\,\nabla\cdot\mathbf{\Omega}_n, \tag{11}$$

where the unit normal $\hat{\mathbf{n}}$ points away from $\mathcal{V}$. If we use this unit normal to orient the surface $\mathcal{S}$, then, according to Eq. (4), the left-hand side equals $2\pi C_n(\mathcal{S})$, and, using Eq. (10), the right-hand side becomes the total Berry flux pumped into band

n from PNs connecting to band $n+1$ above, minus the total Berry flux sucked into band $n-1$ from PNs connecting to band $n-1$,

$$C_n(\mathcal{S}) = \sum_{W_{n\alpha}\in\mathcal{V}} \chi_{n\alpha} - \sum_{W_{n-1,\alpha}\in\mathcal{V}} \chi_{n-1,\alpha}. \tag{12}$$

In the context of Eq. (5) we can apply the divergence theorem to the BZ subvolume between two parallel slices. Because the fluxes through the side faces cancel out in pairs, this gives the difference between the Chern numbers on the top and bottom slices as the sum of the chiral charges in between. For slices separated by $\Delta k_z = 2\pi/a$ the periodicity condition (6) implies that

$$\sum_{\alpha} \chi_{n\alpha} - \sum_{\alpha} \chi_{n-1,\alpha} = 0, \tag{13}$$

where the sum is now over PNs in the full BZ. Repeating the argument for Eq. (7) we obtain a stronger sum rule for the net charge of all PNs connecting two adjacent bands,

$$\sum_{\alpha} \chi_{n\alpha} = 0. \tag{14}$$

Alternatively, Eq. (14) can be proved by induction starting from Eq. (13), which for $n=1$ gives $\sum_\alpha \chi_{1\alpha} = 0$.

A single PN with $\chi \neq 0$ cannot be eliminated from the band structure by varying a control parameter, as this would violate the above "charge neutrality" condition. A chiral node can only appear or disappear as part of a concerted chirality-conserving event, as for example when two WPs of opposite chirality merge and annihilate. Chiral degeneracies can be detected by measuring the quantized Berry flux coming out of a small enclosing box. If a box $\mathcal{S}$ encloses a single node of charge $\chi_{n\alpha}$ then, according to Eqs. (4) and (12),

$$\chi_{n\alpha} = \frac{1}{2\pi} \oint_{\mathcal{S}} dS\hat{\mathbf{n}} \cdot \boldsymbol{\Omega}_n(\mathbf{k}). \tag{15}$$

C. Lines of degeneracy (line nodes)

Line nodes can be thought of as "flux tubes" carrying a quantized Berry flux of π. That is, the Berry phase of Eq. (2) around any small loop $\mathcal{C}$ encircling the line node is equal to π [40,41]. Line nodes do not carry a net chiral charge and are therefore less robust than chiral PNs against translationally invariant perturbations. They are often "protected" by crystal symmetries, and lowering the symmetry can gap the line node almost everywhere (possibly leaving behind a few PNs whose charges sum up to zero).

III. FERMI-SURFACE CHERN NUMBERS

A. Definitions

We now turn our attention to the Chern numbers of Fermi sheets and their relationship to the populations of enclosed chiral PNs. We are considering a metal with a spin-split FS as a result of broken inversion or time-reversal symmetry (or more precisely, broken PT symmetry). In our nomenclature the "FS" S_n of band n is the full set of points $E_n(\mathbf{k}) = E_F$, while the "Fermi sheet" S_{na} is the ath connected piece of the FS. (Here "connectedness" is defined without reference to the BZ boundaries, so that a Fermi pocket centered at a zone corner is a single Fermi sheet.) Note that S_{na} separates a region of occupation $f = n-1$ from a region of occupation $f = n$. The Chern number of S_{na} is, according to Eq. (4),

$$C_{na} = \frac{1}{2\pi} \oint_{S_{na}} dS\hat{\mathbf{v}}_F \cdot \boldsymbol{\Omega}_n(\mathbf{k}), \tag{16}$$

where we have chosen $\hat{\mathbf{v}}_F$ as the unit normal to S_{na}, i.e., parallel to the Fermi velocity and pointing toward the higher-energy side, which is unoccupied in band n.

Throughout this section we assume that all Fermi sheets are isolated, as is required, in principle, in order to define their Chern numbers from Eq. (16). While this is the generic case for a ferromagnet in the absence of any symmetry [6], bcc Fe magnetized along [001] has a mirror plane at $k_z = 0$ and, as we shall see, some Fermi sheets are glued together at isolated points on that plane. The implications for the calculated Chern numbers are discussed in Sec. VI B 3.

In order to proceed, we need notions of "interior" and "exterior." By definition, the *exterior* is the side pointed to by $\hat{\mathbf{v}}_F$ (the unoccupied side), while the *interior* is the occupied side. This can sometimes be counterintuitive, as for a hole pocket, where the interior defined here is the geometric exterior and vice versa. If S_{na}, when regarded all by itself, divides the BZ into two distinct connected regions, we define these regions to be the *global* interior and exterior:

$$I^*_{na} = \text{global interior of } S_{na},$$
$$E^*_{na} = \text{global exterior of } S_{na}.$$

To illustrate this, consider Fig. 1(a), which shows a BZ with three Fermi sheets separating band 1 from band 2; these are labeled S_{21}, S_{22}, and S_{23}. So, for example, I^*_{21} is the union of regions B, C, and D, while E^*_{23} is the union of A, B, and C.

There may be some sheets, however, for which the concepts of global interior and exterior are not applicable. Consider, for example, either one of the sheets shown in Fig. 1(b). Such Fermi sheets are of the special kind having a "Luttinger anomaly" as discussed around Eq. (7) in Ref. [6] and have the property that the integrated unit normal $\oint \hat{\mathbf{v}}_F\, dS$ is nonzero. These "directed sheets" need special treatment. We take the approach here of pairing them. That is, we take the two adjacent directed sheets S_{21} and S_{22} in Fig. 1(b) and henceforth consider them to comprise a single "Fermi sheet" whose global interior is A and whose global exterior is B. Henceforth, the notation S_{na} can refer either to a single nondirected sheet or to a pair of oppositely directed sheets.

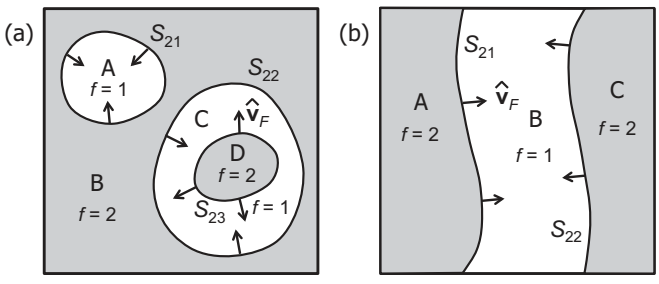

FIG. 1. Examples of Fermi-sheet structures.

It is also useful to have a notion of *immediate* interior and exterior:

$$I_{na} = \text{immediate interior of } S_{na},$$
$$E_{na} = \text{immediate exterior of } S_{na}.$$

To define the immediate interior, we decompose the subspace of the BZ in which band n is occupied into a set of disjoint subvolumes, each of which is internally connected; call these V_{nj}, where j runs over the number of disjoint subvolumes. Similarly, let $\widetilde{V}_{nj}$ be the disjoint subvolumes making up the unoccupied part of the BZ for band n. Together, the V_{nj} and $\widetilde{V}_{nj}$ cover the BZ once and only once. The immediate interior of S_{na} is then just the subvolume V_{nj} that is immediately adjacent to S_{na}. More precisely, it is the region V_{nj} for which $S_{na} \in \delta V_{nj}$, where δ means "the boundary of." (In general, δV_{nj} may consist of several Fermi sheets, one of which is S_{na}.) A similar definition applies to the "immediate exterior," which is the subvolume $\widetilde{V}_{nj}$ adjacent to S_{na}. In Fig. 1(a), for example, the immediate exterior E_{21} of sheet S_{21} is region A (it is geometrically on the inside because it is a hole pocket). The immediate interior of S_{21} is region B only. The immediate interior of S_{22} is also region B, while its immediate exterior is only region C, and so on.

Before continuing, we briefly note that there are two ways of thinking about the volumes V_{nj}. In one point of view, the nominal boundaries of the BZ are ignored, so that, for example, an electron pocket centered on a zone corner point is regarded as a single volume, and all boundaries of the V_{nj} are Fermi sheets. This is the viewpoint adopted in the present section. Alternatively, one can first establish a choice of parallelepiped or Wigner-Seitz BZ, and decompose the interiors and exteriors into subregions within this BZ, so that the δV_{nj} generally also include patches of the BZ boundary. We adopt the latter viewpoint when discussing one of the FS formulations of the AHC in Sec. IV B, where application of the divergence theorem requires the specification of definite BZ boundaries.

B. Divergence theorem using global regions

Because δI^*_{na} has only one connected piece, namely S_{na}, we can apply the divergence theorem to find [see Eq. (12)]

$$C_{na} = \sum_{W_{n\alpha} \in I^*_{na}} \chi_{n\alpha} - \sum_{W_{n-1,\alpha} \in I^*_{na}} \chi_{n-1,\alpha}. \tag{17}$$

A similar argument applied to the global exterior implies that

$$C_{na} = -\sum_{W_{n\alpha} \in E^*_{na}} \chi_{n\alpha} + \sum_{W_{n-1,\alpha} \in E^*_{na}} \chi_{n-1,\alpha}. \tag{18}$$

The reversal of signs between these two equations is due to the fact that, for $\mathcal{V} = I^*_{na}$ in Eq. (11), we have $\hat{\mathbf{n}} = \hat{\mathbf{v}}_F$ on the left-hand side, while for $\mathcal{V} = I^*_{na}$ we have $\hat{\mathbf{n}} = -\hat{\mathbf{v}}_F$. In view of the sum rule of Eq. (14), Eqs. (17) and (18) are consistent with each other; we can use either one to compute the Chern number from the PNs, depending on which is easier.

C. Divergence theorem using immediate regions

We can apply the divergence theorem to an arbitrary connected subvolume V_{nj} or $\widetilde{V}_{nj}$, obtaining

$$\sum_{S_{n\alpha} \in \delta V_{nj}} C_{na} = \sum_{W_{n\alpha} \in V_{nj}} \chi_{n\alpha} - \sum_{W_{n-1,\alpha} \in V_{nj}} \chi_{n-1,\alpha} \tag{19}$$

or

$$\sum_{S_{n\alpha} \in \delta \widetilde{V}_{nj}} C_{na} = -\sum_{W_{n\alpha} \in \widetilde{V}_{nj}} \chi_{na} + \sum_{W_{n-1,\alpha} \in \widetilde{V}_{nj}} \chi_{n-1,\alpha}. \tag{20}$$

Unfortunately, these equations do not immediately determine the FS Chern numbers unless the boundary of the region in question is composed of only a single sheet.

For example, applying Eq. (19) to subvolume B in Fig. 1(a) leaves the sum of two Chern numbers ($C_{21} + C_{22}$) on the right-hand side, so neither can be determined directly. However, in cases like this an iterative analysis will typically work; for example, applying Eq. (20) to region A determines C_{21}, and, together with the previous result, this also determines C_{22}.

A similar problem arises in Fig. 1(b), but now it is more serious. Recall that we agreed to pair directed sheets; having done so, we can apply Eq. (19) and obtain the total Chern number summed over the two subsheets. However, now there is no way to disentangle the Chern numbers on the individual directed subsheets without an additional calculation. This does not necessarily have to be done on the actual subsheet; in Fig. 1(b), for example, a calculation on one planar surface lying between the two directed sheets would suffice.

D. Sum rules on Chern numbers

Summing Eq. (19) or (20) over all n and all subvolumes, we obtain the sum rule

$$\sum_{na} C_{na} = 0, \tag{21}$$

which, as Haldane points out, must be satisfied on gauge-invariance grounds [6,21].

When P symmetry is present (but T is broken) the sum rule holds for each band separately,

$$\sum_{a} C_{na} = 0. \tag{22}$$

This follows from combining Eqs. (A1) and (A3) with either Eq. (19) or Eq. (20): For every PN at $\mathbf{k}$, there is a partner at $-\mathbf{k}$ with the same energy but opposite charge. If, moreover, a Fermi sheet S_{na} encloses a parity-invariant momentum $\mathbf{k}_0 = \mathbf{G}/2$, then $C_{na} = 0$.

IV. ANOMALOUS HALL CONDUCTIVITY

The role played by degeneracies in the intrinsic AHC has been recently debated [26,29] in connection with FS formulations [21,30]. This debate probably has its roots in the simplifying assumption, made more or less explicitly at certain points in Refs. [21] and [30], that the band under consideration is everywhere nondegenerate. Instances where this isolated-band assumption was made in Ref. [21] include the sentence below Eq. (12), and also Eq. (20); examples in Ref. [30] are the sentence below Eq. (7) and most of Sec. II B.

In this section we show that the FS formulations of Refs. [21] and [30] remain valid when the chiral degeneracies that are generally present in the occupied band manifold are carefully accounted for. To be precise, the nonquantized part of the intrinsic AHC is still given by the same bulk FS expressions derived in those works. The presence of isolated PNs carrying topological charges does *not* lead to additional nonquantized, non-FS contributions to the AHC, as claimed in Ref. [26].

A. Fermi-sea formulation

The AHC of a 3D crystal is conveniently expressed as

$$\sigma_{ij} = -\frac{e^2}{2\pi h} \sum_{l=x,y,z} \epsilon_{ijl} K_l, \tag{23}$$

where e^2/h is the quantum of conductance and $\mathbf{K}$ is a wave vector. When the Fermi level lies in an energy gap, $\mathbf{K}$ becomes quantized to a reciprocal lattice vector $\mathbf{G}$ [21,36].

Specializing to the intrinsic (Karplus-Luttinger) contribution, we can work band by band and write

$$\mathbf{K} = \sum_n \mathbf{K}_n. \tag{24}$$

The contribution from band n is

$$\mathbf{K}_n = \frac{1}{2\pi} \int_{I_n} d^3k \boldsymbol{\Omega}_n(\mathbf{k}), \tag{25}$$

where the Berry curvature $\boldsymbol{\Omega}_n(\mathbf{k})$ is given by Eq. (3) and $I_n = \cup_a I_{na}$ is the BZ region where band n is occupied. Equations (23)–(25) form the standard Fermi-sea expression for the intrinsic AHC [42,43].

While it is natural to view $\mathbf{K}_n$ as "the intrinsic AHC contributed by band n," it should be kept in mind that each $\mathbf{K}_n$ by itself is not a physical observable; only the total $\mathbf{K}$ is. For example, the individual $\mathbf{K}_n$ are not invariant under arbitrary band-mixing gauge transformations within the occupied band manifold. In the next section we discuss an alternative decomposition due to Haldane [21], Eq. (34) below, that is equally valid and in some ways more informative than Eq. (24).

B. Haldane's Fermi-surface formulation

1. Dipole of the chiral-charge distribution in k space

Let us rewrite Eq. (25) using an integration by parts of the form

$$\int_{\mathcal{V}} dV (\boldsymbol{\nabla} g) \cdot \boldsymbol{\Omega}_n = \oint_{\delta\mathcal{V}} dS \hat{\mathbf{n}} \cdot g \boldsymbol{\Omega}_n - \int_{\mathcal{V}} dV g \boldsymbol{\nabla} \cdot \boldsymbol{\Omega}_n, \tag{26}$$

which follows from replacing $\boldsymbol{\Omega}_n(\mathbf{k})$ with $g(\mathbf{k})\boldsymbol{\Omega}_n(\mathbf{k})$ in Eq. (11). Setting $\mathcal{V} = I_n$, $g = k_i$, and using Eq. (10) we find

$$\mathbf{K}_n = \mathbf{K}_n^{(\Omega)} + \mathbf{K}_n^{(\chi)}, \tag{27}$$

$$\mathbf{K}_n^{(\Omega)} = \frac{1}{2\pi} \oint_{\delta I_n} d^2k \mathbf{k} [\hat{\mathbf{n}} \cdot \boldsymbol{\Omega}_n(\mathbf{k})], \tag{28}$$

$$\mathbf{K}_n^{(\chi)} = \sum_{W_{n-1,\alpha} \in I_n} \mathbf{k}_{n-1,\alpha} \chi_{n-1,\alpha} - \sum_{W_{n\alpha} \in I_n} \mathbf{k}_{n\alpha} \chi_{n\alpha}. \tag{29}$$

These equations express $\mathbf{K}_n$ as the dipole moment of a distribution of chiral charge inside the BZ [44]. $\mathbf{K}_n^{(\chi)}$ is the contribution from the discrete charges associated with the occupied PNs, and $\mathbf{K}_n^{(\Omega)}$ is the contribution from a continuous distribution of charge across the surface δI_n [with $\hat{\mathbf{n}} \cdot \boldsymbol{\Omega}_n(\mathbf{k})/2\pi$ playing the role of an areal density of "bound chiral charge"].

We now adopt the second point of view described at the end of Sec. III A, in which the boundary δI_n generally consists of FS sheets S_{na} together with the portions of the BZ boundary (BZB) where band n is occupied; this is demanded by the presence of the linear term $\mathbf{k}$ in Eq. (28). We choose a parallelepiped BZ, as opposed to a Wigner-Seitz one, to ensure a simple relation between opposing faces. Thus, the surface integral in Eq. (28) runs over portions of the BZB, as well as over the Fermi sheets per se. Explicitly,

$$\mathbf{K}_n^{(\Omega)} = \sum_a \mathbf{K}_{na}^{(\Omega)} + \mathbf{K}_{n,\mathrm{BZB}}^{(\Omega)}, \tag{30}$$

where

$$\mathbf{K}_{na}^{(\Omega)} = \frac{1}{2\pi} \oint_{S_{na}} d^2k \mathbf{k} [\hat{\mathbf{v}}_F \cdot \boldsymbol{\Omega}_n(\mathbf{k})] \tag{31}$$

is the contribution from the ath Fermi sheet and

$$\mathbf{K}_{n,\mathrm{BZB}}^{(\Omega)} = \frac{1}{2\pi} \oint_{\mathrm{BZB}_n} d^2k \mathbf{k} [\hat{\mathbf{n}} \cdot \boldsymbol{\Omega}_n(\mathbf{k})] \tag{32}$$

is the contribution from the portions of the BZB where band n is occupied, denoted by BZB_n. In this last equation $\hat{\mathbf{n}}$ points to the outside of the BZ.

Equation (27) differs from Eq. (20) in Haldane's Ref. [21] in that the latter does not include the term $\mathbf{K}_n^{(\chi)}$. This extra term appears when the band has PN degeneracies and is needed to ensure that the cell dipole $\mathbf{K}_n$ remains invariant when the origin in k space is shifted. Under a shift of $-\delta\mathbf{k}$, Eq. (27) changes by

$$\delta\mathbf{K}_n = \delta\mathbf{k} \left[\sum_a C_{na} + \sum_{W_{n-1,\alpha} \in I_n} \chi_{n-1,\alpha} - \sum_{W_{n\alpha} \in I_n} \chi_{n\alpha} \right], \tag{33}$$

where C_{na} is the Fermi-sheet Chern number defined in Eq. (16), and $\delta\mathbf{K}_{n,\mathrm{BZB}}^{(\Omega)} = 0$ due to canceling contributions from opposing BZ faces. The quantity in square brackets vanishes by virtue of Eq. (19).

In some cases the volume and surface chiral-charge distributions are separately neutral. This happens for a completely filled band in a generic crystal [Eq. (13)] and for any band in a centrosymmetric crystal [Eq. (22)]. Even then, the two separate terms in Eq. (27) are not fully invariant under another type of transformation: a rigid shift of the BZ cell. Consider what happens when a PN with $\chi_{n\alpha} = +1$ leaves the BZ on one side and reenters on the opposite side, at a point separated by $-\mathbf{G}$ from the exit point: $\mathbf{K}_n^{(\chi)}$ given by Eq. (29) jumps by $\mathbf{G}$, and it will become clear in a moment that $\mathbf{K}_{n,\mathrm{BZB}}^{(\Omega)}$ changes by $-\mathbf{G}$.

To summarize, the situation is as follows.

(i) The AHC contribution from band n is most naturally defined as the integral of the Berry curvature over the occupied portion of the band, as in Eq. (25).

(ii) The contribution from band n can be expressed as $\mathbf{K}_n = \mathbf{K}_n^{(\Omega)} + \mathbf{K}_n^{(\chi)}$, where the inclusion of the $\mathbf{K}_n^{(\chi)}$ term is needed to preserve the invariance of $\mathbf{K}_n$ under an origin shift, or under a shift of the BZ cell.

(iii) As we shall see shortly, $\mathbf{K}_n^{(\Omega)}$ is quantized for any fully occupied band. On the other hand, $\mathbf{K}_n^{(\chi)}$, and hence $\mathbf{K}_n$, has a nonquantized contribution even for a completely filled band if the band in question has chiral degeneracies with higher or lower bands.

(iv) Nevertheless, the $\mathbf{K}_n^{(\chi)}$ contributions from Eq. (29) add up to zero when summing over all bands [46]. Hence,

$$\mathbf{K} = \sum_n \mathbf{K}_n^{(\Omega)} \tag{34}$$

correctly gives the total AHC, in a way that the nonquantized part of $\mathbf{K}$ is now ascribed exclusively to the partially filled bands.

Let us reexamine the conclusions of Ref. [26] in the light of the preceding discussion. Essentially the claim, stated in the Abstract, is that when chiral degeneracies are present in the Fermi sea, the nonquantized part of the AHC is not entirely a (bulk) FS property. In the main text, the authors purport to show that the additional nonquantized, non-FS contributions originate in the chiral PNs of the completely filled bands.

If taken at face value, the above statements would seem to imply that a purely FS formulation of the nonquantized AHC is not possible. However, this cannot be correct, since the nonquantized part of $\mathbf{K}$ can be completely ascribed to the partially filled bands by means of Eq. (34), even when chiral degeneracies are present. The nonquantized part of $\mathbf{K}$ can, moreover, be expressed as a bulk FS property, as shown below following Haldane's original argument [21]. In their analysis, the authors of Ref. [26] appear to have overlooked the fact that the nonquantized Fermi-sea contributions $\mathbf{K}_n^{(\chi)}$ from the occupied PNs sum up to zero over all bands.

2. *Fermi-surface expression for* $\mathbf{K}_n^{(\Omega)}$

In Ref. [21], Haldane further manipulated his Eq. (20) [our Eq. (28)] to arrive at his Eq. (21), in which the BZB term was written in a more explicit form. For completeness, we repeat this derivation here using our notation.

We choose a parallelepiped BZ defined by a triplet of primitive reciprocal lattice vectors $\mathbf{b}_j$, such that the reduced coordinate $\kappa_j = (\mathbf{a}_j \cdot \mathbf{k})/2\pi$ goes from κ_{j0} to $\kappa_{j0}+1$ inside the BZ, where κ_{j0} fixes the corner of the BZ cell. Recalling that the integration in Eq. (32) runs over the portions of the six BZ faces where band n is occupied, we can decompose the BZB term into contributions from the three sets of opposing faces according to

$$\mathbf{K}_{n,\mathrm{BZB}}^{(\Omega)} = \sum_{j=1}^{3} \mathcal{K}_{nj}^{\mathrm{BZB}} \mathbf{b}_j, \tag{35}$$

obtaining

$$\mathcal{K}_{nj}^{\mathrm{BZB}} = \frac{1}{2\pi} \oint_{\mathrm{BZB}_n} d^2k \kappa_j \hat{\mathbf{n}} \cdot \boldsymbol{\Omega}_n(\mathbf{k}). \tag{36}$$

When computing $\mathcal{K}_{nj}^{\mathrm{BZB}}$, the integrations on the four side surfaces of the BZB cancel in pairs, while the contributions from the surfaces related by $\mathbf{b}_j$ fail to cancel because of the κ_j factor. The result is

$$\mathcal{K}_{nj}^{\mathrm{BZB}} = \frac{1}{2\pi} \int_{\mathcal{B}_{nj}} d^2k \hat{\mathbf{a}}_j \cdot \boldsymbol{\Omega}_n(\mathbf{k}), \tag{37}$$

where $\mathcal{B}_{nj}$ is the portion of the BZB at $\kappa_j = \kappa_{j0}+1$ that is occupied in band n, and $\hat{\mathbf{a}}_j$ is the outward unit normal. In the notation of Eq. (8), $\mathcal{K}_{nj}^{\mathrm{BZB}}$ is $1/2\pi$ times the Berry flux,

$$\phi_{nj} = \int_{\mathcal{B}_{nj}} d^2k \hat{\mathbf{a}}_j \cdot \boldsymbol{\Omega}_n(\mathbf{k}), \tag{38}$$

exiting the BZ cell through the occupied portions of the BZ face pointed to by $\mathbf{b}_j$.

If band n is fully occupied, $\mathcal{K}_{nj}^{\mathrm{BZB}}$ is just the Chern number obtained by integrating the Berry curvature over the entire BZ face in direction j. If the band is also isolated, the integers $\mathcal{K}_{nj}^{\mathrm{BZB}}$ are independent of the choice of cell origin $\boldsymbol{\kappa}_0$, and $\mathbf{K}_{n,\mathrm{BZB}}^{(\Omega)}$ is a unique "Chern vector" $\sum_j \mathcal{K}_{nj}^{\mathrm{BZB}} \mathbf{b}_j$ describing the topology of the filled band. If it is fully occupied but not isolated, $\mathcal{K}_{nj}^{\mathrm{BZB}}$ is still quantized to be a triplet of integers, but these may change discontinuously if $\boldsymbol{\kappa}_0$ is shifted in such a way that one of the BZ boundaries passes over a chiral PN. If band n is only partially occupied, then the integral in Eq. (37) is only over the occupied portions of the BZ face at $\kappa_j = \kappa_{j0}+1$, and $\mathcal{K}_{nj}^{\mathrm{BZB}}$ need not be an integer.

To summarize so far, Eq. (34) has become

$$\mathbf{K} = \sum_{na} \mathbf{K}_{na}^{(\Omega)} + \frac{1}{2\pi} \sum_{nj} \mathbf{b}_j \phi_{nj}, \tag{39}$$

where $\mathbf{K}_{na}^{(\Omega)}$ is the $\mathbf{k}$-weighted integral of the surface-normal Berry curvature on sheet S_{na}, Eq. (31), and ϕ_{nj} is the Berry flux passing through the occupied portion $\mathcal{B}_{nj}$ of the BZ face, Eq. (38). After summing over all bands there is no ambiguity modulo a quantum in either of the contributions above, and Eq. (39) correctly gives the total intrinsic AHC modulo nothing. Equation (39) is still not quite a FS property, because the ϕ_{nj} have to be obtained by integrating over portions of the band lying at energies below E_F on the BZB.

In order to arrive at Eq. (21) of Haldane's Ref. [21], we now abandon the goal of computing the AHC exactly and only ask for its nonquantized part. Two modifications can be made to Eq. (39) that only affect the result by quantized amounts and lead to a FS expression for the nonquantized part of $\mathbf{K}$. First, the sums over n can be restricted to partially occupied bands, recalling that completely filled bands only contribute to the second term and by a quantized amount. The second is to invoke Eq. (9) in order to replace the Berry fluxes ϕ_{nj} with sums of Berry phases that are only defined modulo 2π,

$$\varphi_{naj} = \oint_{\mathcal{C}_{naj}} d\mathbf{k} \cdot \mathbf{A}_n(\mathbf{k}). \tag{40}$$

The oriented curve $\mathcal{C}_{naj}$ consists of one or more planar circuits at the intersections of the sheet S_{na} with the BZ face at $\kappa_j = \kappa_{j0}+1$, so that $\cup_a \mathcal{C}_{naj} = \delta\mathcal{B}_{nj}$. If we view the BZ face as an open parallelogram with edges, those circuits may include non-FS segments along the edges. If instead we view it as a closed 2-torus, a nonvanishing $\mathcal{C}_{naj}$ consists exclusively of Fermi loops and we arrive at Haldane's FS expression, Eq. (21)

of Ref. [21], in the form

$$\mathbf{K} := \sum_{na}{}' \mathbf{K}_{na}^{(\Omega)} + \frac{1}{2\pi} \sum_{naj}{}' \mathbf{b}_j \varphi_{naj}, \tag{41}$$

where a prime on a sum indicates that n only runs over bands crossing E_F. The symbol := indicates that the quantity on the left-hand side is equal to the right-hand side modulo a reciprocal lattice vector $\mathbf{G}$. Since the Berry phases φ_{naj} are defined for loops lying on the FS, this is now a true FS property.

C. Tomographic Fermi-surface formulation

Equation (41) for the nonquantized part of the AHC involves Berry curvatures on the Fermi sheets as well as Berry phases around Fermi loops on the BZB. An alternative FS formula was obtained in Ref. [47] that only involves Berry phases. In this section we recover this Fermi-loop expression starting from Eq. (41). The present derivation is therefore complementary to the one given in Ref. [47], which starts from the Fermi-sea formulation of Sec. IV A and does not make an explicit connection to Haldane's expression.

We work sheet by sheet, treating each sheet as one connected piece. Sheets with nonzero Chern numbers are grouped together in such a way that their combined Chern number vanishes. This is needed to obtain an AHC contribution that is origin-independent in the sense of Eq. (33). Thus, in the following S_{na} denotes either a single sheet with $C_{na} = 0$ or a group of sheets whose Chern numbers add up to zero.

Writing the contribution from S_{na} to Eq. (41) as

$$\mathbf{K}_{na} = \sum_{j=1}^{3} \mathcal{K}_{naj} \mathbf{b}_j, \tag{42}$$

we find

$$2\pi \mathcal{K}_{naj} = \int_{S_{na}} d^2k \kappa_j \hat{\mathbf{v}}_F \cdot \boldsymbol{\Omega}_n(\mathbf{k}) + \oint_{\mathcal{C}_{naj}} d\mathbf{k} \cdot \mathbf{A}_n(\mathbf{k}). \tag{43}$$

If the sheet is holelike, the Fermi loops $\mathcal{C}_{naj}$ should be traversed in the negative direction of circulation.

Recalling the interpretation of Eq. (27) as a dipole moment in k space, we can similarly view the first term in Eq. (43) as an intracell dipole moment of a surface distribution of bound chiral charge and the second term as an intercell "charge-transfer" term. Separately, each term depends on the choice of cell vectors and on the placement of the cell boundaries, but their sum is independent of those arbitrary choices.

Since the total $\mathcal{K}_{naj}$ given by Eq. (43) is cell invariant, we are allowed to average the right-hand-side over several different BZ cells. We choose for this purpose the range of cells obtained by sliding a parallelepiped BZ along the full length of its edge $\mathbf{b}_j$. The dipole term then averages to zero (because the net charge per cell C_{na} vanishes), and we are left with the average of the intercell term. As the cell slides over one period, the forward-facing boundary cuts through an entire BZ, producing a tomographic scan of the Fermi sheet. The contribution from each slice (viewed as a 2-torus) is given by the Berry phases of the inscribed Fermi loops. Averaging over a discrete set of slices spanning the entire BZ we find

$$\mathcal{K}_{naj} = \frac{1}{n_{\text{slice}}} \sum_{i=1}^{n_{\text{slice}}} \frac{\varphi_{naj}(i)}{2\pi}, \tag{44}$$

and summing over all Fermi sheets we recover the FS expression in Ref. [30] for the nonquantized AHC,

$$\mathcal{K}_j := \sum_{na}{}' \mathcal{K}_{naj}. \tag{45}$$

Equations (44) and (45) must be supplemented with a prescription for choosing the branch cuts of the Berry phases. The allowed choices are strongly constrained by the BZ-averaging procedure: the first term in Eq. (43) changes continuously with the position of the BZ cell (because the "bound chiral charge" is spread across the sheet S_{na}), and this should be exactly balanced by the change in the second term. Thus, φ_{naj} must change gradually (by much less than 2π) from one slice to the next. Note that enforcing smoothness only fixes the branch cut on a slice relative to that on the previous slice. The freedom to choose the branch cut on the first slice leaves the integer part of $\mathcal{K}_{naj}$ undetermined, as expected of a FS formulation.

After summing Eq. (44) over the indices n and a, the overall quantum of indeterminacy can be resolved by equating $\sum_{na} \varphi_{naj}$ with the total Berry flux $\sum_n \phi_{nj}$ on the first slice (a Fermi-sea quantity) [30]. It is, however, not always possible to similarly resolve the quantum for the AHC contribution from an *individual* Fermi sheet S_{na}. If the sheet encloses chiral PNs, the integer part of $\mathcal{K}_{naj}$ obtained by anchoring the Berry phase φ_{naj} on the first slice to the Berry flux ϕ_{naj} will depend on where that slice stands relative to those PNs.

For a composite sheet comprising several disconnected pieces, φ_{naj} changes by $2\pi C_\alpha$, while traversing a single piece S_α with Chern number C_α [29]. If we fix the branch choice by arbitrarily setting $\varphi_{naj} = 0$ below the first piece, φ_{naj} reaches $2\pi C_1$ at the top of that piece, remains constant until hitting the next piece, and finally drops back to zero at the top of the last piece. We encounter this type of behavior when studying the AHC of bcc Fe in Sec. VI C.

V. COMPUTATIONAL DETAILS

A. First-principles calculations and Wannier-function construction

Our electronic structure calculations including SOC are carried out for ferromagnetic Fe in the bcc structure. We fix the lattice constant at the experimental value $a = 5.42$ bohr and orient the magnetization along the easy axis [001]. (That is, minority and majority spins point up and down respectively.) In reality, α-Fe distorts very slightly from bcc to body-centered tetragonal on cooling through the magnetic transition, but we ignore this lattice strain effect and set $c/a = 1$ in our calculations.

We use the plane-wave pseudopotential method as implemented in the PWSCF code from the QUANTUM-ESPRESSO package [48], in a noncollinear spin framework. Relativistic norm-conserving pseudopotentials are generated from parameters similar to those in Ref. [47], and an energy cutoff of 120 Ry is used for the plane-wave expansion of the wave functions. Exchange and correlation effects are treated within

the Perdew-Burke-Ernzerhof (PBE) generalized-gradient approximation [49]. The self-consistent total energy calculations are done with a $16 \times 16 \times 16$ Monkhorst-Pack mesh for the BZ integration, while for the non-self-consistent calculations a $10 \times 10 \times 10$ mesh is used. A Fermi smearing of 0.02 Ry is used during the self-consistent cycle, and the 28 lowest bands are calculated in the non-self-consistent step.

Starting from the Bloch functions computed in the non-self-consistent step, maximally localized Wannier functions [50,51] are constructed using the WANNIER90 code [52]. The choice of trial orbitals and energy windows is the same as in Refs. [47] and [30], resulting in 18 partially occupied spinor Wannier functions. We also carry out some SOC-free calculations where nine Wannier functions are generated separately for each spin channel.

B. Berry phases, curvatures, and Chern numbers

For the evaluation of Berry curvatures and Berry phases in k space we use the efficient Wannier-interpolation algorithms of Refs. [47] and [30]. In this section we focus on the aspects that are specific to the present work and refer the reader to those papers for other details.

We begin by describing how to compute the slice Chern number $C_n(k_z)$ of Eq. (5) [the same approach is used for the slice Chern number $\widetilde{C}_n(k_z)$ of Eq. (7) and also for the box Chern number of Eq. (15)]. The most direct approach would be to evaluate the Berry curvature on a k-point mesh covering the 2D BZ. The disadvantage is that for any finite mesh the result is not exactly quantized, and we have encountered situations where the deviations were significant even for very dense meshes (this can happen close to critical k_z values where the true Chern number changes discontinuously).

The interpretation of the Berry curvature as a Berry phase per unit area suggests an alternative strategy: Tile the 2D BZ with square plaquettes, and compute the Berry phases $\varphi_n^{\square}(k_z)$ around their edges [53]. The Chern number is

$$C_n(k_z) = \frac{1}{2\pi} \sum_{\square}^{\text{2D BZ}} \varphi_n^{\square}(k_z), \tag{46}$$

where the plaquette Berry phase $\varphi_n^{\square}(k_z)$ is evaluated with the discretized Berry-phase formula [54] on a counterclockwise path consisting of its four corners. In our implementation we use the Wannier-based version of the discretized Berry-phase formula, Eq. (25) in Ref. [30]. [In the case of $\widetilde{C}_n(k_z)$ the multiband generalization [54] of the second term in that equation should be used instead.] Note that because each link along the discretized path is traversed twice in opposite directions when evaluating Eq. (46), the net contribution from the first term in Eq. (25) of Ref. [30] vanishes identically.

The above prescription is guaranteed to give an integer result for $C_n(k_z)$ for arbitrary lattice spacings [53]. The correct Chern number is obtained by choosing each Berry phase $\varphi_n^{\square}(k_z)$ in the principal branch between $-\pi$ and π, provided that the magnitude of the Berry-curvature flux through every plaquette is safely below π. In practice, we start by tiling the 2D BZ with a uniform array of equally sized plaquettes (e.g., 200×200), and whenever $|\varphi_n^{\square}(k_z)| > \pi/3$ for some plaquette we divide it into subplaquettes so as to meet the above requirement [55]. The slice Chern number is then obtained by summing the Berry phases over all (sub)plaquettes covering the 2D BZ. Care must be taken to ensure that every link is traversed twice, once in each direction. If, for example, a plaquette has been divided into four subplaquettes but a neighboring plaquette has not, then when computing the Berry phase for the larger plaquette the middle point of the shared edge should be included in the discretized path along with the four corner points.

We use the same algorithm to determine the Berry flux through the occupied portions of a BZ slice, Eq. (38). For a partially filled band the flux is not quantized, and the first term in Eq. (25) of Ref. [30] must be included; because the links along the edge between occupied and empty regions are traversed only once, that term gives a net contribution. As far as the nonquantized part of the Berry flux is concerned (i.e., the Berry phase around the Fermi loops), this approach is equivalent to integrating the Berry connection over a ragged path at the edge approximating the Fermi loops. For improved numerical accuracy, we triangulate the edge with new k points chosen to approximate the location of the Fermi loops; this changes the shape of the plaquettes along the edge from squares to triangles or irregular quadrilaterals.

VI. NUMERICAL RESULTS FOR BCC IRON

A. Band degeneracies

1. Overview of the spinor band structure

Our electronic structure calculations including SOC are carried out for ferromagnetic Fe in the bcc structure, as discussed in Sec. V A. The energy bands, shown in Fig. 2, are in good agreement with previous band-structure calculations for bcc Fe where SOC was included [34,56,57]. The smaller exchange splitting at the band bottom (at around -8 eV) compared to Ref. [56] is a consequence of using the PBE generalized-gradient approximation rather than the local-density approximation to treat exchange and correlation effects.

Even though an undistorted cubic structure is used, the combined action of spin polarization and SOC reduces the

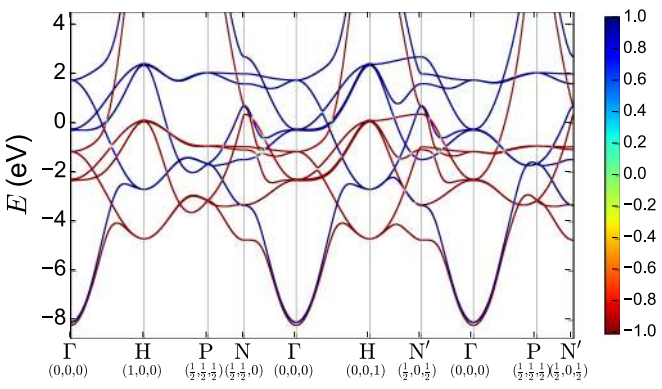

FIG. 2. (Color online) Band structure of bcc Fe with SOC included. Energies are measured from the Fermi level, and the bands are color coded by the expectation value of the spin component S_z in units of $\hbar/2$, ranging from red (majority down-spin character) to blue (minority up-spin), as indicated by the color bar.

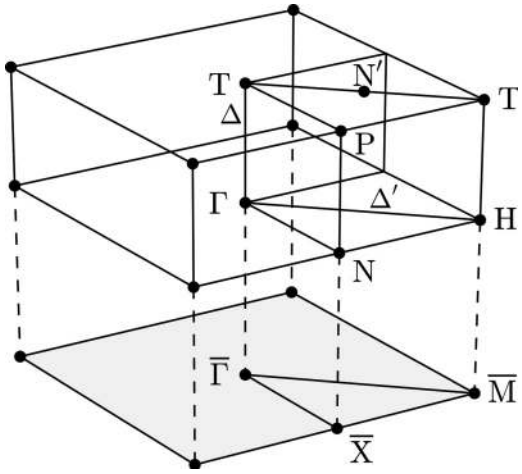

FIG. 3. Symmetry points and lines in reciprocal space for bcc Fe with SOC included. The top volume is the half BZ between $k_z = 0$ and $k_z = \pi/a$ (which becomes a full BZ when expanded using inversion through Γ). The shaded area at the bottom is a 2D projection. Therein, $\overline{\Gamma}$ is a projection of Γ-T-H-T-Γ (Δ), $\overline{\mathrm{X}}$ is a projection of N-P-N-P-N, and $\overline{\mathrm{M}}$ is a projection of H-T-Γ-T-H. Note that T is not actually a symmetry point, but N′ is.

symmetry of the electronic states from cubic to tetragonal, and the conventional labeling scheme for the high-symmetry points and lines in the BZ must be modified accordingly. For example, the six points N inside the BZ get split into two groups. We reserve the label N for the two points lying on the $k_z = 0$ plane, and label the four points lying on the $k_z = \pi/a$ plane as N′; within each separate group, symmetry points are related to one another by fourfold rotations. The ΓH high-symmetry line along the (001) direction also becomes inequivalent to the other two, since it is no longer related to them by any point-group symmetry; we label them Δ and Δ′, respectively. The symmetry points and lines are indicated in the half-BZ shown in the top part of Fig. 3. The full tetragonal BZ is spanned by the vectors $(2\pi/a)(1\bar{1}0)$, $(2\pi/a)(110)$, and $(2\pi/a)(001)$. Note that only the first two are reciprocal-lattice vectors.

The lowering of symmetry due to SOC is reflected in the band structure in Fig. 2, but since SOC is weak the effect is small on the scale of the figure. As we see in Sec. VI B 1, somewhat larger splittings occur away from the symmetry lines [56].

2. Types of degeneracies

Band degeneracies can be classified as *essential* or *accidental* [58]. An essential degeneracy is a band crossing at a high-symmetry point or along a high-symmetry line in the BZ where an irreducible representation ("irrep") of dimension larger than one exists. It has been shown that essential degeneracies do not occur in the band structure of tetragonal ferromagnets when SOC is included [18–20]. Thus, all band degeneracies in bcc Fe are accidental. While their exact locations in k space are not fixed by symmetry, most (but not all) degeneracies in bcc Fe lie along symmetry lines or planes in the BZ. Below we give an overview of the types of accidental degeneracies that are present, classified by symmetry (they are, in fact, the generic types of degeneracies in any tetragonal ferromagnet).

The magnetic point group of bcc Fe is $4/mm'm'$ [20]. The fourfold axis points along the magnetization direction [001], and m denotes mirror reflection about the (001) plane orthogonal to the fourfold axis. The symmetry elements m' are reflections about the inequivalent vertical planes (010) and (110), combined with time reversal.

Turning to the symmetries in reciprocal space, inspection of Fig. 3 reveals fourfold symmetry about the axis Δ that projects onto $\overline{\Gamma}$ and also about the one that projects onto $\overline{\mathrm{M}}$ [59]. At an arbitrary point on one of the fourfold axes no other symmetries are present when SOC is included, and each band belongs to one of four 1D irreps of the little group C_4; bands belonging to different irreps can cross, so that for critical values of k_z (not fixed by symmetry) PNs are generated.

The four irreps along the fourfold axes are labeled by their symmetry eigenvalues $e^{i\pi(m+1/2)/2}$, and the labels of the crossing bands carry information about the chiral charge at the degeneracy point [16]. Two types of degeneracies can occur. (i) If the two bands have adjacent labels on the complex unit circle, they disperse linearly in all directions away from the degeneracy point; the chirality of the WP is positive ($\chi_{n\alpha} = +1$) if the label of the lower band n changes by a factor of i with increasing k_z, and negative ($\chi_{n\alpha} = -1$) if it changes by a factor of $-i$. (ii) If the labels are not adjacent, the crossing is a double-Weyl node with $\chi_{n\alpha} = \pm 2$, where the dispersion away from the node is linear along the symmetry axis and quadratic on the orthogonal plane; in this case, the sign of the chiral charge cannot be inferred from the symmetry labels alone.

The axis that projects onto $\overline{\mathrm{X}}$ is a twofold axis, where there are two 1D irreps (little group C_2). Along this axis, crossings between bands belonging to different irreps are always linear ($\chi_{n\alpha} = \pm 1$), but the chirality of the WP cannot be deduced from the symmetry labels [16].

A different type of degeneracy occurs on the simple mirror plane at $k_z = 0$, i.e., the ΓNH plane in Fig. 3. (Equivalent planes are separated by integer multiples of $2\pi/a$; because the structure is body centered, the plane TPN′ at $k_z = \pi/a$ is not a mirror plane.) There can be no chiral PN degeneracies on a simple mirror plane, because the chiral charge is odd under reflection [Eq. (A10)]. Instead, the generic degeneracies are nonchiral nodal rings. The spinor energy eigenstates carry mirror symmetry labels $\pm i$; bands with different labels can cross, and since the condition $E_{n\mathbf{k}} = E_{n+1,\mathbf{k}}$ is one constraint for the two degrees of freedom k_x and k_y, the crossing takes place along lines.

Next we consider the vertical symmetry planes ΓN′H, ΓNP, and HNP that project onto the lines $\overline{\Gamma}\,\overline{\mathrm{M}}$, $\overline{\Gamma}\,\overline{\mathrm{X}}$, and $\overline{\mathrm{X}}\,\overline{\mathrm{M}}$, respectively. In real space these are m' planes (mirror composed with T), but because of the time-reversal component, a generic point on the reciprocal-space plane is not invariant under m'. Instead, the symmetry operations that leave the wave-vector invariant (modulo $\mathbf{G}$) on those planes are of the form C_2T, where C_2 is a twofold rotation about an axis normal to the plane. Because the C_2T operator is antiunitary it does not admit multiple irreps, and so does not lead to nodal rings as in the case of simple mirror planes. However, it does place additional restrictions on the form of the Hamiltonian on the plane. In particular, it forces

the Hamiltonian matrix to be real when expressed in terms of symmetry-adapted Bloch basis orbitals $|\chi_{n\mathbf{k}}\rangle$ whose phases are chosen such that $C_2T|\chi_{n\mathbf{k}}\rangle = |\chi_{n\mathbf{k}}\rangle$. Since degeneracies occur with codimension two for real Hamiltonians, WPs generically occur on the symmetry plane [60].

Finally, we encounter one more type of degeneracy, namely those occurring at generic points in the interior of the BZ. Here a division into distinct irreps again plays no role, since no symmetry is present. One still gets isolated touchings, in general, however, because the codimension is three for the occurrence of degeneracies in Hermitian Hamiltonians. That is, by adjusting the wave vectors (k_x,k_y,k_z) one can generically zero the prefactors of the Pauli matrices $(\sigma_1,\sigma_2,\sigma_3)$ needed to express the effective Hamiltonian in the vicinity of a putative crossing of two bands. In the absence of fine tuning, these are always simple Weyl nodes with a chiral charge of ± 1.

We emphasize that all of the above considerations apply when SOC is present. When it is neglected, additional degeneracies can occur, as discussed briefly in Sec. VI B 1.

3. *Survey of degeneracies*

We have used a combination of numerical tools to locate and characterize the degeneracies in the spinor band structure of bcc Fe. In this section we present some representative results from our survey.

In order to locate all the degeneracies between a pair of bands, we carry out a steepest-descent minimization of the gap function $(E_{n+1,\mathbf{k}} - E_{n\mathbf{k}})^2$, starting from a uniform grid covering the BZ, and look for gap-closing points [62]. (In practice, we flag as a potential degeneracy any point where the gap is below some small threshold, of the order of 10^{-5} eV.) The chiral charge of each degeneracy is determined by enclosing it in a small box and evaluating the outward Berry flux [Eq. (15)]; in this way, we are able to discriminate between a true chiral band crossing with nonzero quantized flux and a tiny avoided crossing for which the flux vanishes. Figure 4 shows a map of the degeneracies between bands six and seven in the half-BZ of Fig. 3.

In addition to finding isolated degeneracies, the above procedure results in a rather dense set of nonchiral degeneracies between bands six and seven lying on the mirror plane at $k_z = 0$. These are organized along closed loops, consistent with the line-node scenario of Sec. II C. In order to confirm that they are nodal rings protected by mirror symmetry, we have performed two separate numerical tests. First we checked that these are true crossings between states belonging to different irreps, by plotting in Fig. 5 the mirror-symmetry label of band six across the $k_z = 0$ plane. The boundaries between regions of different symmetry (the gray and white regions) coincide with the locus of degeneracies of band six with either band seven or band five, indicated with lines. For example, when going between a gray and a white region across a thick (red) line, bands six and seven cross with one another and exchange symmetry labels.

The second test was to determine the Berry flux carried by each ring. To this end we evaluated numerically the Berry phases of small circular loops interlinked with the rings, obtaining the value π expected for nodal rings. Note that the sign of the Berry phase of a mirror-symmetric vertical loop is flipped by the mirror operation, but because the Berry phase is only defined modulo 2π, the nontrivial value π is still allowed.

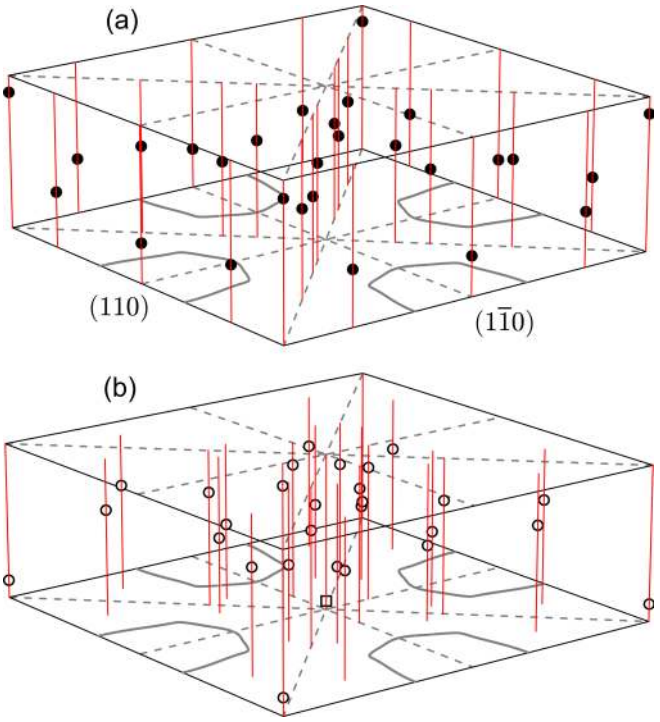

FIG. 4. (Color online) Degeneracies between bands six and seven in the half BZ of Fig. 3. (a) Black dots denote WPs of positive chirality (monopole sources of Berry curvature on band six). (b) Open circles denote WPs of negative chirality, and the single open square represents a negative double-Weyl node. Each chiral degeneracy is threaded by a vertical line to help locate it with respect to the projected high-symmetry lines (dashed gray lines). The solid gray lines on the $k_z = 0$ plane represent nonchiral nodal rings.

Recently, the FSs of several T-invariant crystals (some P broken [7,8], others P invariant [64,65]) were found to consist of nodal rings on mirror planes, but only when SOC is absent. Those Fermi rings are crossings between *pairs* of spin-degenerate bands, and SOC hybridizes the states of opposite spin, gapping the rings everywhere except at a few isolated points despite the unbroken mirror symmetry [8,65]. In bcc Fe the spin degeneracy is lifted by the exchange interaction, removing the hybridization channels and stabilizing the nodal rings against SOC (except when SOC destroys the mirror symmetry itself, e.g., on the vertical symmetry planes).

Let us now analyze the isolated degeneracies away from the $k_z = 0$ plane in Fig. 4. There are 45 in total in the half-BZ, and except for a double-Weyl node along the fourfold axis Δ all of them are simple WPs. Their properties are listed in Table I. Each row represents one or more symmetry-related PNs lying on the same BZ slice at fixed k_z, and their multiplicity (one, two, four, or eight) is determined by the projection onto the 2D BZ at the bottom of Fig. 3. Multiplicities of two and four are generated by C_4 symmetry, and multiplicities of eight are generated by C_4 symmetry together with C_2T symmetry about the vertical symmetry planes. A mirror-equivalent set of nodes, but with reversed chiral charges, appears in the $k_z < 0$ half of the BZ.

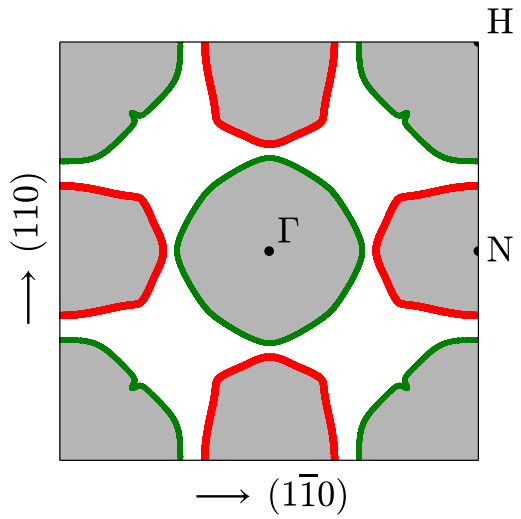

FIG. 5. (Color online) Mirror symmetry labels ($+i$ in gray and $-i$ in white) of band six on the mirror plane at $k_z = 0$. The degeneracy lines of band six with bands five and seven are drawn in thin (green) and thick (red) lines, respectively.

The degeneracies between bands six and seven realize almost all possibilities that can generically exist in a tetragonal ferromagnet: Nodes of chiral charge ± 1 that project onto $\overline{\Gamma}$ or $\overline{\mathrm{M}}$ (multiplicity one), $\overline{\mathrm{X}}$ (multiplicity two), $\overline{\Gamma}\,\overline{\mathrm{M}}$, $\overline{\Gamma}\,\overline{\mathrm{X}}$, or $\overline{\mathrm{X}}\,\overline{\mathrm{M}}$ (multiplicity four), or generic points (multiplicity eight); and nodes of chiral charge ± 2 projecting onto $\overline{\Gamma}$ or $\overline{\mathrm{M}}$. Only the very last possibility is missing between bands six and seven in Table I, but an opposite-spin crossing of this type occurs, for example, between bands four and five at $k_z \simeq 0.376 \times 2\pi/a$.

The correctness of the PN assignments in Table I is confirmed in Fig. 6, where we plot between $k_z = 0$ and $k_z = \pi/a$ the joint slice Chern number $\widetilde{C}$ [Eq. (7)] of the six lowest bands. Each step discontinuity signals the presence on the corresponding BZ slice of one or more chiral PNs connecting bands six and seven. The positions of the steps match the k_z coordinates listed in Table I, and their sizes satisfy

$$\Delta\widetilde{C} = (\text{multiplicity}) \times (\text{chiral charge}) \tag{47}$$

for the chiral charges and multiplicities in Table I.

Let us contrast the behavior of the energy bands and symmetry labels in the vicinity of a simple WP and of a double-Weyl node, when both lie along fourfold axes. Figure 7 pertains to the WP at $k_z \simeq 0.446$ projecting onto $\overline{\mathrm{M}}$. The top

TABLE I. Census of chiral degeneracies between bands six and seven in the half BZ of Figs. 3 and 4. The coordinates (k_x,k_y,k_z) are in units of $2\pi/a$; energy E is in eV relative to the Fermi level. "Proj." indicates the projection onto the 2D BZ at fixed k_z (bottom of Fig. 3; "gen." is a generic point). The last three columns indicate spin crossing type ($\downarrow$ and $\uparrow$ are majority and minority spins, respectively), chiral charge ($\chi > 0$ if the band touching is a source of Berry curvature on band six), and multiplicity within the 2D BZ.

k_x	k_y	k_z	Proj.	E	Spin	χ	Mult.
0.0	0.0	0.027	$\overline{\Gamma}$	−1.16	$\downarrow\downarrow$	−2	1
0.0	1.0	0.056	$\overline{\mathrm{M}}$	0.06	$\downarrow\downarrow$	−1	1
0.5	0.5	0.130	$\overline{\mathrm{X}}$	−0.96	$\downarrow\downarrow$	+1	2
0.180	0.820	0.180	$\overline{\mathrm{X}}\,\overline{\mathrm{M}}$	−0.34	$\sim\downarrow\downarrow$	+1	4
0.074	0.322	0.242	gen.	−1.01	$\uparrow\downarrow$	−1	8
0.0	0.327	0.243	$\overline{\Gamma}\,\overline{\mathrm{M}}$	−0.99	$\uparrow\downarrow$	+1	4
0.0	0.583	0.284	$\overline{\Gamma}\,\overline{\mathrm{M}}$	−0.87	$\downarrow\downarrow$	+1	4
0.0	0.217	0.316	$\overline{\Gamma}\,\overline{\mathrm{M}}$	−0.99	$\uparrow\uparrow$	+1	4
0.135	0.662	0.338	gen.	−1.07	$\downarrow\downarrow$	−1	8
0.0	0.365	0.365	$\overline{\Gamma}\,\overline{\mathrm{M}}$	−1.02	$\uparrow\uparrow$	−1	4
0.118	0.118	0.429	$\overline{\Gamma}\,\overline{\mathrm{X}}$	−0.84	$\uparrow\downarrow$	−1	4
0.0	1.0	0.446	$\overline{\mathrm{M}}$	−0.94	$\uparrow\downarrow$	+1	1

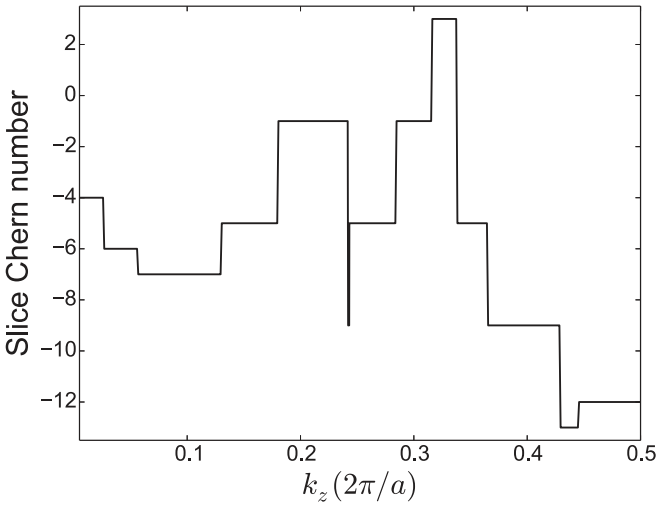

FIG. 6. Slice Chern number $\widetilde{C}$ [Eq. (7)] associated with the six lowest bands of bcc Fe. Since $\widetilde{C}$ is symmetric about $k_z = 0$ and $k_z = \pi/a$ [Eqs. (A4) and (A5)], only half of the range of k_z is shown.

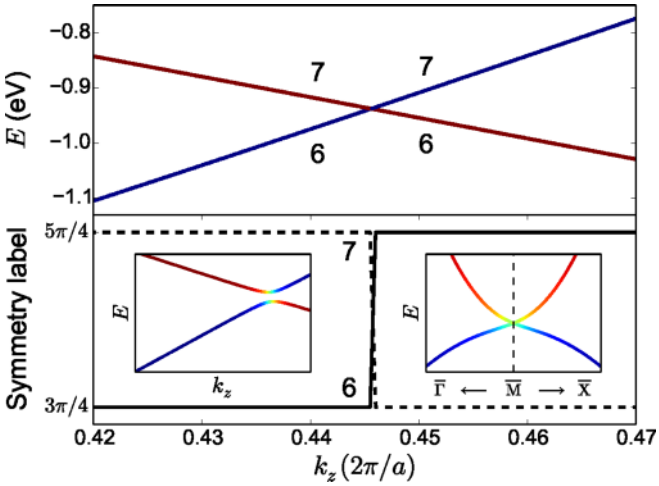

FIG. 7. (Color online) A WP between bands six and seven along the fourfold axis that projects onto $\overline{\mathrm{M}}$ in Fig. 3. The top panel and the right inset show the band dispersions as one passes through the touching point along the symmetry axis and on the orthogonal plane, respectively. The left inset shows the dispersion along a vertical line that is shifted from the symmetry axis by $\delta k_x = 0.05 \times 2\pi/a$. The bands are color coded by the spin as in Fig. 2. The main bottom panel shows the evolution along the symmetry axis of the phase of the C_4 eigenvalues (symmetry labels) of the crossing bands.

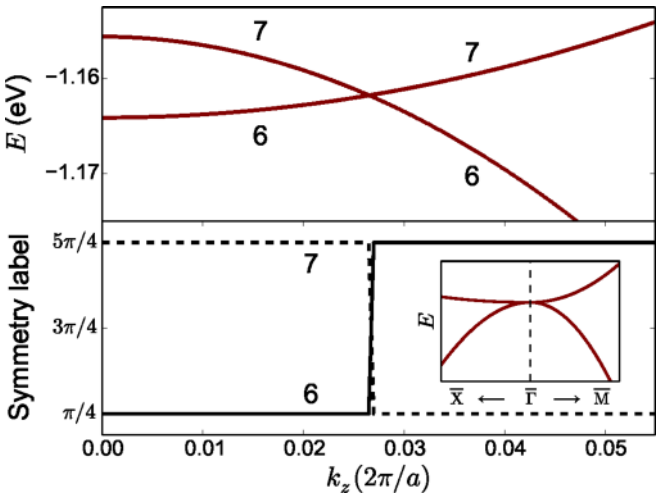

FIG. 8. (Color online) A double-Weyl node between bands six and seven along the fourfold axis Δ in Fig. 3. The top and bottom panels and the right inset have the same meaning as in Fig. 7. Near the crossing the two bands have majority-spin character, as indicated by the red color.

and bottom panels show, respectively, the linearly dispersing bands and the evolution of the symmetry labels along the symmetry axis. As expected for a WP of positive chirality, the label of the lower band changes by a factor of i at the crossing [16]. Exactly at the crossing the two bands retain their separate spin characters, but moving slightly away from $\overline{\mathrm{M}}$ (left inset) they hybridize and no longer touch. The right inset shows that the bands also disperse linearly away from the touching point in the orthogonal directions (the leading behavior is linear even though strong nonlinearities are present), but now with strong spin mixing near the crossing. The behavior around the double-Weyl node on the Δ axis is shown in Fig. 8, and it is qualitatively different. Here the bands still disperse linearly away from the node along the axis, but the dispersion is quadratic on the orthogonal plane at the critical k_z. Moreover, the symmetry labels of the crossing bands are noncontiguous on the complex unit circle [16].

This concludes our survey of the degeneracies between bands six and seven; other bands display the same basic types of degeneracies. For future reference we list in Table II the chiral degeneracies between bands nine and ten.

TABLE II. Census of chiral degeneracies between bands nine and ten in the half BZ of Fig. 3. The table is organized in the same way as Table I.

k_x	k_y	k_z	Proj.	E	Spin	χ	Mult.
0.0	1.0	0.047	$\overline{\mathrm{M}}$	2.35	↑↑	+1	1
0.0	0.0	0.065	$\overline{\Gamma}$	−0.25	↑↑	+1	1
0.188	0.812	0.188	$\overline{\mathrm{X}}\,\overline{\mathrm{M}}$	1.85	↑↑	−1	4
0.322	0.322	0.331	$\overline{\Gamma}\,\overline{\mathrm{X}}$	1.81	↑↓	+1	4
0.0	0.0	0.428	$\overline{\Gamma}$	−0.06	↑↑	−1	1
0.233	0.233	0.446	$\overline{\Gamma}\,\overline{\mathrm{X}}$	1.39	↑↑	−1	4
0.0	0.0	0.480	$\overline{\Gamma}$	0.07	∼↑↑	+2	1

B. Fermi surface

1. Overview and spin-orbit effects

We begin by analyzing the FS of bcc Fe with SOC switched off. Callaway and co-workers [34,66] introduced a labeling scheme for the Fermi sheets that has been widely adopted in the literature. The sheets are organized into eight groups. In a calculation without SOC the majority-spin Fermi sheets belong to groups I–IV, and the minority-spin sheets belong to groups V–VIII. Figure 9(a) shows the labeled Fermi contours on the mirror plane at $k_z = 0$. We now consider the possible touchings and intersections between Fermi sheets, starting with the SOC-free case.

Crossings between Fermi sheets of opposite spin occur along entire loops in the 3D BZ where the two constrains $E_{n\uparrow}(\mathbf{k}) = E_{m\downarrow}(\mathbf{k}) = E_F$ are satisfied. Some of those loops intersect the portion of the $k_z = 0$ plane shown in Fig. 9(a), at the six points where sheets I or II (red) cross V or VIII (blue).

Touchings between like-spin Fermi sheets can occur along lines of degeneracy, at the isolated points where the degeneracy energy E_{degen} equals E_F. Four such contact points can be seen in Fig. 9(a). Two are linear touchings between majority-spin sheets I and II, and they are located along nodal rings (the curved gray lines) connecting bands five and six on the mirror plane [67]. Each nodal ring changes from a solid line ($E_{\mathrm{degen}} < E_F$) to a dashed line ($E_{\mathrm{degen}} > E_F$) at the Fermi touching points, and the band indices of the two Fermi sheets that touch tell which bands are degenerate along a given ring. The other two are quadratic touchings, one between sheets III and IV for majority spins and the other between sheets V and VII for minority spins. Both of them lie on the dash-dotted gray line Δ′ from Γ to H, where there is an essential degeneracy between pairs of bands in each spin channel (without SOC the little group along Δ′ is C_{4v}, which has a 2D irrep). The bands close to the Fermi level are plotted along Δ′ in Fig. 9(b). Note that the essential degeneracy is between bands two and three near Γ, and between bands three and four near H.

There is one more opportunity for like-spin Fermi touchings, namely at generic points in the BZ along nodal rings located away from any symmetry lines or planes: The removal of SOC restores an effective T symmetry in each spin channel, which combined with parity produces an effective PT symmetry protecting such rings [41,64]. Several low-symmetry nodal rings are present in the band structure near the Fermi level, but none of them cross E_F. For example, they occur below E_F between majority-spin bands three and four and also five and six, and between minority-spin bands two and three, and above E_F between minority-spin bands four and five.

Now we turn to the FS with SOC included. Figure 10 shows the calculated FS in the 3D BZ. Each Fermi sheet is labeled S_{na} as in Sec. III, and sheets with the same band index n are displayed together. The unoccupied sides are colored in blue, and the occupied sides in yellow/gold. Thus, the pockets in bands five to seven are holelike, and so is the connected tubular structure in band eight, while the pockets in bands nine and ten are electronlike.

The spin-orbit interaction changes both the symmetry and the connectivity of the FS, and its organization into groups of symmetry-related sheets must be modified accordingly.

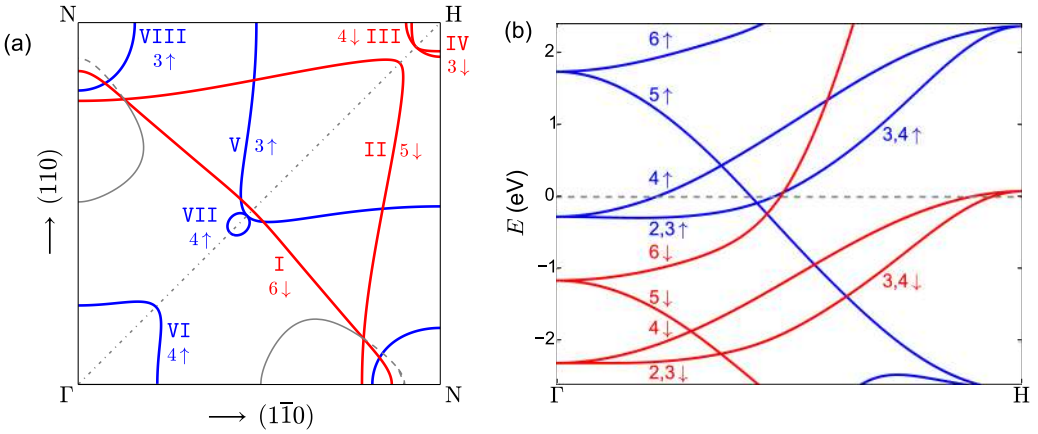

FIG. 9. (Color online) (a) Fermi contours of bcc Fe on the ΓNH plane at $k_z = 0$, calculated without SOC. The majority-spin contours I–IV are in red; the minority-spin contours V–VIII in blue. Curved gray lines are accidental degeneracy lines (nodal rings) that cross the Fermi level at points of contact between like-spin Fermi sheets, where they change from solid ($E_{\text{degen}} < E_F$) to dashed ($E_{\text{degen}} > E_F$). The dashed-dotted line from Γ to H is a line of essential degeneracy. (b) Energy bands close to the Fermi level along the ΓH line. In both panels, the spin-dependent band indices are indicated.

Without SOC, group VIII comprises the six pockets surrounding each of the points N in the BZ (the centers of the faces of the Wigner-Seitz cell in Fig. 10). With SOC, this group splits in two: group VIII(a) formed by the four pockets surrounding the points N′ in Fig. 3 [sheets two to five in Fig. 10(c)] and group VIII(b) containing the two pockets surrounding the points N [sheets six and seven in Fig. 10(c)].

The other group that gets split by SOC is group VII comprising the six "satellite" electron pockets in band ten. The four pockets along the lines Δ′ in Fig. 3 [pockets two to five in Fig. 10(f)] remain related by C_4 symmetry, so we group them together as VII(a). Pockets six and seven along Δ are no longer related by symmetry to the other four; they are, however, related to each other by both parity and mirror reflection, and we label them VII(b).

Figure 11(a) displays the Fermi contours on the $k_z = 0$ plane. The contours are labeled as in Fig. 1, but using the more compact notation n_a instead of S_{na}. (The correspondence with the labels for groups of symmetry-related Fermi sheets is given in Table III.) Comparison with Fig. 9(a) shows that some, but not all, of the gluing points between Fermi sheets have been removed by SOC, with sizable gaps opening up in some cases. In particular, the quadratic touching between sheets III and IV along Δ′ has been lifted, and the one between sheets V and VII turned into a pair of linear crossings between the pair $(9,10_2)$ on either side of Δ′.

Generic Fermi-sheet touchings require a locus of band degeneracies of dimension $d \geqslant 1$ since the additional constraint $E_{\text{degen}} = E_F$ reduces the dimensionality by one, and with SOC the only eligible degeneracies are nodal rings on the $k_z = 0$ plane. The nodal rings connecting bands six and seven in Figs. 4 and 5 lie entirely below E_F and thus play no role here. However, several nodal rings lying on the $k_z = 0$ plane do cross E_F, as indicated by the solid/dashed gray curves in Fig. 11(b). The ones labeled α, β_1, and β_2 are degeneracy loops between bands seven and eight; α glues sheet 8 to sheet 7_1 at eight points, while β_1 and β_2 provide gluings to sheets 7_6 and 7_7 at four points each. Ring γ provides eight points of contact between sheets 8 and 9, and ring δ connects sheet 9 twice to each of 10_2, 10_3, 10_4, and 10_5. We thus see that it is quite common for Fermi sheets to be glued to one another on the $k_z = 0$ plane in bcc Fe. The gluing together of Fermi sheets is protected by mirror symmetry, and hence it does not require fine tuning. By tuning external parameters, it is also possible to arrange for sheets to touch away from the $k_z = 0$ plane. Two examples are discussed in Secs. VI B 3 and VI C 2.

The situation is very different on the $k_y = 0$ plane of Fig. 12, which is not a mirror plane with SOC present. No actual Fermi touchings occur there, although some of the avoided crossings are very small and difficult to discern on the scale of the figure. In particular, what look like two touchings between sheets (8,9) in the lower half of the figure are, in fact, tiny avoided crossings, as becomes clear in Sec. VI C.

2. *Fermi-sheet Chern numbers*

Without SOC all the band degeneracies in bcc Fe are nonchiral, the Berry curvature vanishes identically, and as a result the FS is topologically trivial. As we have seen, the inclusion of SOC generates chiral band touchings that act as sources and sinks of Berry curvature. We now determine the Chern numbers induced on the Fermi sheets from the census of chiral PNs, as described in Sec. III. For isolated Fermi sheets the Chern number is unique and is correctly obtained from this census. For those that are glued to neighboring ones by nodal rings lying on the $k_z = 0$ plane, on the other hand, it provides only part of the story. The true sheet Chern number is ill defined until the symmetry protecting the nodal rings is broken, and when it is, the sheet Chern number may have additional contributions from new PNs that appear at special points along the vaporized nodal ring. This is discussed in Sec. VI B 3.

We use the formulation of Sec. III C, based on the PN population in "immediate regions." (Since no Luttinger anomalies are present, the special treatment that is required in such cases is not needed here.) Inspection of Fig. 10 shows that, for each Fermi sheet, it is possible to identify an occupied or empty connected BZ region having that Fermi sheet as the

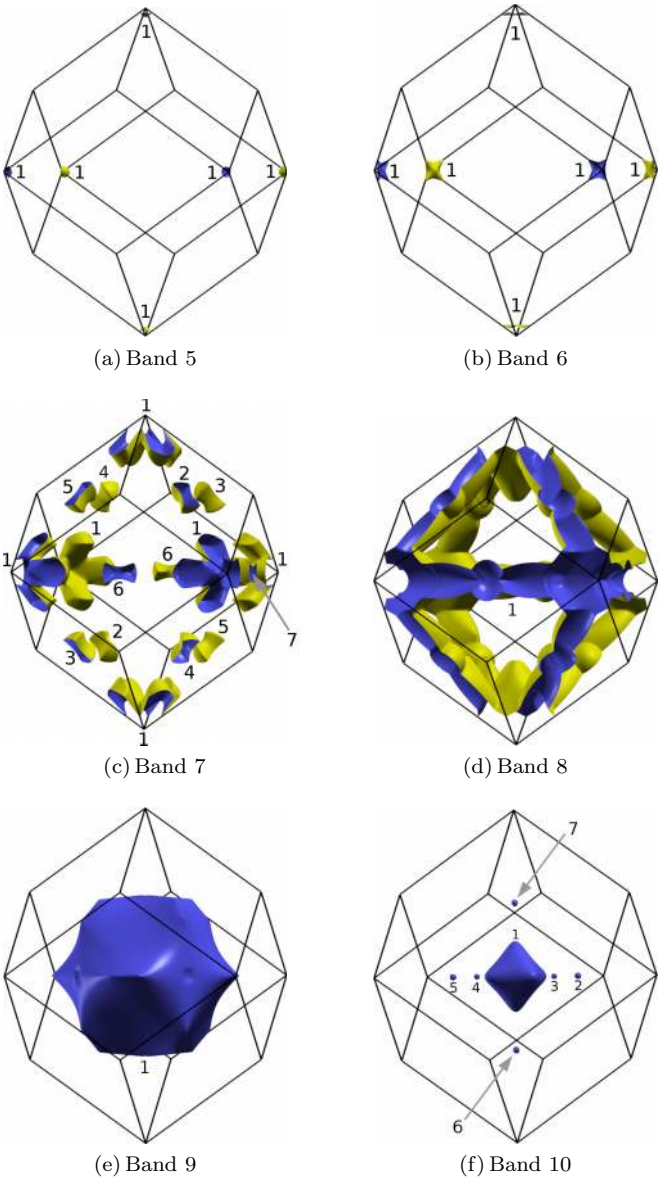

(a) Band 5 (b) Band 6

(c) Band 7 (d) Band 8

(e) Band 9 (f) Band 10

FIG. 10. (Color online) Fermi surface of bcc Fe with SOC included. The indices a of the individual Fermi sheets S_{na} on each band n are indicated.

sole boundary. For the holelike sheets of band seven that means working with exteriorlike regions, while for the electronlike sheets of band ten it means working with interiorlike regions; bands five, six, eight, and nine have a single sheet each, so that either approach can be used (in practice, we choose the one leading to the smallest number of enclosed PNs). In this way we are able to determine the Chern number of each Fermi sheet from a single evaluation of either Eq. (19) or Eq. (20), without the need for a recursive procedure.

Our implementation of Eq. (19) for electron pockets is as follows. In order to determine the internally connected occupied subvolumes V_{nj}, we cover the BZ with a uniform $300 \times 300 \times 300$ grid and set up an undirected graph with nodes at those grid points where band n is occupied, and whose edges are the links to the nearest-neighbor points that are also occupied. The problem becomes a standard one in graph theory, namely, to identify the connected components of an undirected graph. Once the subvolumes V_{nj} have been identified in this way (the algorithm "wraps around" the BZ, so that the BZ boundaries are excluded from the definition of δV_{nj}), we go through the list of occupied PNs $W_{n\alpha}$ and $W_{n-1,\alpha}$ and assign each of them to the subvolume V_{nj} containing the closest grid point. This allows us to carry out the summations on the right-hand side of Eq. (19) to determine the Chern number C_{na} of each electron pocket $S_{na} = \delta V_{nj}$. The implementation of Eq. (20) for the holelike Fermi sheets is completely analogous.

The results are summarized in Table III, and several features can be readily understood from symmetry considerations. The vanishing of the Chern numbers summed over all the sheets of any given band is a consequence of inversion symmetry [Eq. (22)], and this explains the values $C_{na} = 0$ for bands six, eight, and nine with one Fermi sheet each (the small hole pocket in band five does not enclose any PNs, and so its Chern number vanishes trivially). According to Sec. III D, in bands with several Fermi sheets inversion symmetry still imposes $C_{na} = 0$ on those which enclose parity-invariant momenta (the points Γ, H, N, and N′ in Fig. 3). This accounts for all sheets in band seven, as well as the central pocket 10_1 in band ten. Note that the vanishing Chern numbers come about in different ways for Fermi sheets belonging to groups VIII(a) and VIII(b) in band seven: The latter do not enclose any PNs, while the former enclose four PNs each with band eight (two inversion-symmetric pairs).

This leaves the six satellite pockets in band ten. The pockets $(10_2, 10_3, 10_4, 10_5)$ located along Δ′ do not enclose any PNs. The pockets $(10_6, 10_7)$, on the other hand, enclose a single WP each. These are touchings with band nine, located along Δ at $k_z = \mp 0.428 \times 2\pi/a$ (see Table II). As their chiralities are reversed by mirror symmetry, the enclosing pockets have opposite Chern numbers ∓ 1.

Figure 13 shows the energy bands near a pocket of type VII(b) [panel (a)], and near one of type VII(a) [panel (b)]. Upon lowering the Fermi level the electron pocket 10_7 in panel (a) will shrink, eventually turning into a hole pocket in band nine with the same Chern number $+1$. The situation with pocket 10_2 in panel (b) is less clear, because of the degeneracy between bands nine and ten near the bottom of band ten. That degeneracy can be lifted by tilting the magnetization in certain directions (those for which no WPs are left inside the now-isolated pocket, as discussed in Sec. VI B 3). Under those conditions pocket 10_2 simply disappears as E_F dips below the bottom of band ten; because its Chern number vanishes, this does not violate the sum rule of Eq. (21).

In order to understand how the two satellite pockets along Δ become different from the four along Δ′ when SOC is included, and why nonzero Chern numbers are induced on the former but not the latter, it is instructive to follow the evolution of the relevant bands in Figs. 13(a) and 13(b) as SOC is turned on. In the SOC-free limit bands eight to ten [corresponding to minority-spin bands two to four in Fig. 9(b)] behave identically along Δ and Δ′, with a doubly degenerate band (eight and nine on the left, nine and ten on the right) crossing a singly-degenerate one (ten on the left, eight on the right). Along Δ in Fig. 13(a), SOC lifts the twofold degeneracy between bands eight and nine, and the crossing of band ten

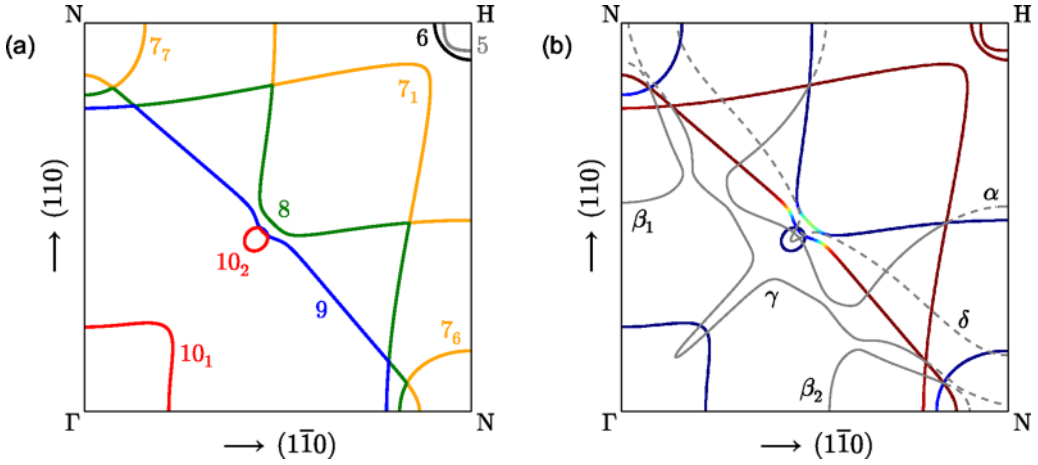

FIG. 11. (Color online) Fermi contours of bcc Fe on the ΓNH plane at $k_z = 0$, with SOC included. (a) The contours are color coded by the band index n and labeled n_a, where a is the sheet index (it is omitted for bands with a single Fermi sheet). (b) The Fermi contours are color coded by the spin in the same way as the energy bands in Fig. 2, and the gray lines labeled α, β_1, β_2, γ, and δ are degeneracy lines (nodal rings) that cross the Fermi level at points of contact between Fermi sheets, where they change from solid ($E_{\text{degen}} < E_F$) to dashed ($E_{\text{degen}} > E_F$).

creates two nearby WPs, with the one between bands nine and ten inducing a Chern number of +1 on the enclosing pocket 10_7. Along Δ' in Fig. 13(b), however, the nature of the hybridization with band ten is very different. While no mirror plane containing Δ survives when SOC is turned on, the M_z mirror plane containing Δ' does survive, and such a plane can only harbor nodal rings, not chiral PNs. The touching between bands nine and ten in Fig. 13(b) belongs to just such a nodal ring; in fact, the same one that appears as ring δ in Fig. 11(b). Since no chiral PNs are enclosed by pocket 10_2, its Chern number vanishes.

TABLE III. Chern numbers of the Fermi sheets of bcc Fe, with SOC included. Symmetry-related Fermi sheets are listed on the same row and are assigned a group label. The Chern numbers are determined from the populations of chiral PNs within "immediate regions," which are exteriorlike (interiorlike) for holelike (electronlike) Fermi sheets. For nonisolated Fermi sheets (labeled by an asterisk), this definition neglects the possible contribution of π fluxes at touching points between Fermi sheets (see Sec. VI B 3). The high-symmetry points enclosed by each Fermi sheet are indicated, and if none are enclosed the symmetry line where the pocket lies is indicated instead. The numbers i, j of enclosed PNs with bands $n-1$ and $n+1$ are also indicated.

Band n	Sheet a	Group label	Type	Enclosed symm. points	Enclosed PNs	Chern number
5	1	IV	Hole	H	0,0	0
6	1	III	Hole	H	0,2	0
7	1	V	Hole	H	2,0	0*
7	2,3,4,5	VIII(a)	Hole	N′	0,4	0
7	6,7	VIII(b)	Hole	N	0,0	0*
8	1	II	Hole	H,N,N′	16,36	0*
9	1	I	Elec.	Γ	42,4	0*
10	1	VI	Elec.	Γ	2,0	0
10	2,3,4,5	VII(a)	Elec.	Along Δ'	0,0	0*
10	6,7	VII(b)	Elec.	Along Δ	1,0	−1,+1

On their own, the pockets $(10_6, 10_7)$ are an almost ideal realization of the simplest T-broken Weyl semimetal. It is therefore natural to ask whether their presence gives rise to "Fermi-arc" surface states connecting their projections onto the surface BZ, as in actual Weyl semimetals. Although we have not explicitly calculated the surface bands of bcc Fe, that seems unlikely: Almost everywhere on the surface BZ there are projected bulk states at the Fermi level coming from all

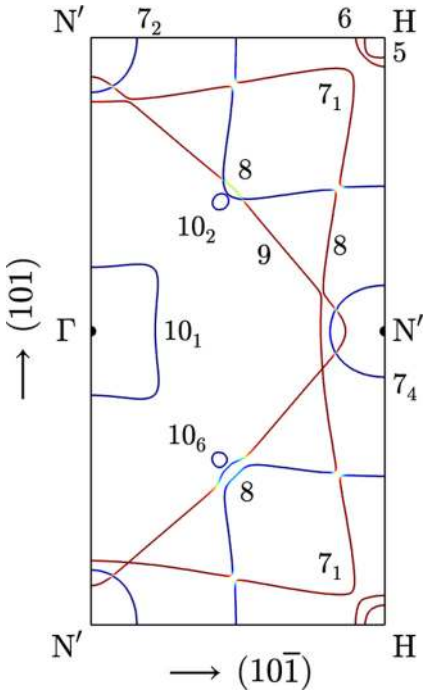

FIG. 12. (Color online) Same as Fig. 11(b), but for the ΓN′H plane at $k_y = 0$. The Fermi contours are labeled in the same way as in Fig. 11(a). Because the symmetry on this plane is reduced by the spin-orbit interaction, the displayed region has twice the area compared to Fig. 11 and there are no symmetry-protected nodal rings.

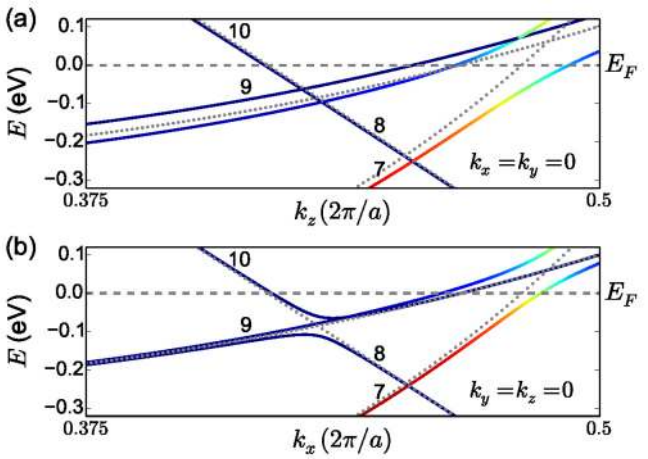

FIG. 13. (Color online) Details of the spinor band structure of Fig. 2. (a) Along the line Δ close to the electron pocket 10_7. (b) Along the line Δ' close to the pocket 10_2. The spin-orbit-free energy bands of Fig. 9 are shown as dotted gray lines.

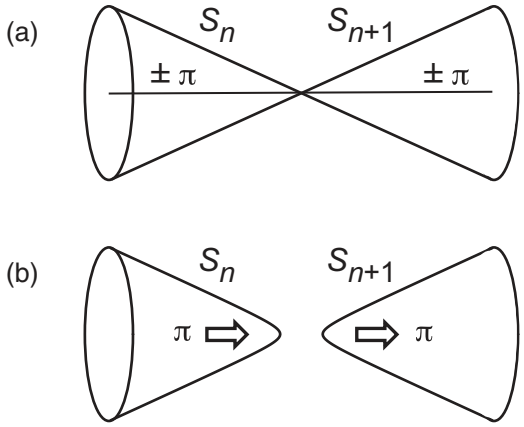

FIG. 14. (a) Gluing together of two Fermi sheets along a symmetry-protected degeneracy line carrying a Berry flux of π modulo 2π, indicated as $\pm\pi$. (b) The symmetry has been broken weakly, gapping the degeneracy line and separating the Fermi sheets. A Berry flux of definite sign now exits one sheet and enters the other.

the other (trivial) Fermi sheets, and their presence destroys the stability of the putative Fermi arcs.

In summary, although chiral degeneracies abound in the spinor band structure of bcc Fe, most Fermi sheets are constrained by symmetry to have zero Chern numbers. The only ones that are free from such constraints are the isolated electron pockets $(10_6, 10_7)$. In our calculation their Chern numbers are ∓ 1, turning bcc Fe into a topologically nontrivial metal.

3. *Chern numbers of nonisolated Fermi sheets*

In Table III we have assigned Chern numbers to all the sheets making up the FS bcc Fe, including those in groups I, II, V, VII(a), and VIII(b) that are glued together along nodal rings lying in the mirror plane [Fig. 11(b)]. For these sheets, the meaning of the assigned Chern number requires a more careful explanation, since Chern numbers are, in principle, only well-defined for isolated Fermi sheets, and they can change when sheets touch as a function of a control parameter.

Figure 14(a) shows a simplified sketch of a generic situation in which Fermi sheets S_n and S_{n+1} are glued together at an isolated "gluing point" where a nodal ring passes through E_F. In our case, the nodal ring lies in the $k_z = 0$ plane and is protected by M_z symmetry. The local two-band $k \cdot p$ Hamiltonian in the vicinity of the touching has a form like

$$H(k'_x, k'_y, k_z) = E_F + \alpha k'_x + \beta k'_y \sigma_3 + \gamma k_z \sigma_1, \qquad (48)$$

where k'_x and k'_y are measured relative to the gluing point and are parallel and normal to the nodal line, respectively, and σ_j are Pauli matrices. The $E = 0$ solutions are conical, as shown in the figure, with the nodal line passing through the conical intersection point. Each nodal line carries a Berry flux of π modulo 2π, which is indicated as $\pm\pi$ in the figure; without breaking the symmetry we cannot say which value applies. The Fermi-sheet Chern numbers reported in Table III correspond to the integral of the Berry curvature over the sheet in question, Eq. (16), but neglecting these possible π-flux contributions. This is the same as the sum of the chiral charges of enclosed PNs that are unrelated to the nodal ring, as will become clear shortly.

Now imagine that the symmetry that was protecting the nodal ring is broken weakly; in our case this can be done by tilting the magnetization **M** away from the tetragonal axis. Then the two bands become gapped everywhere along the path except possibly at PNs along it, corresponding to the addition of a term $\mu(k)\sigma_2$ to Eq. (48), where the argument k is a reminder that μ can vary along the path. Then a definite flux of $+\pi$ or $-\pi$ (depending on the sign of μ) flows along the previous path of the ring, concentrated in a small vicinity (of size proportional to μ) around the path. As shown in Fig. 14(b), the previously glued Fermi sheets now separate and become hyperboloids, and a concentration of π flux now exits one sheet and enters the other. These π-flux contributions must be included when computing the true Chern number of the sheet in the presence of the symmetry breaking.

Note, however, that if the nodal ring enters a given Fermi sheet at one point, it must exit at another, and the total contribution of the π fluxes will be of opposite sign and will cancel unless $\mu(k)$ crosses through zero and changes sign at some special point along the ring, generating a new chiral PN at this location. As long as this PN is included in the census of enclosed PNs, the total Chern number of the sheet will still be correctly given by the sum of enclosed chiral charges.

In order to see how this works out in the present context, we have investigated the consequences of breaking the M_z mirror symmetry, which is responsible for the nodal rings shown in Fig. 11(b). When we tilt **M** away from [001] the nodal rings evaporate, leaving behind a few extra PNs, and the previously glued-together Fermi sheets become detached. We can then safely determine their individual Chern numbers from the populations of enclosed chiral degeneracies (including the newly formed PNs).

Parametrizing the magnetization direction by polar and azimuthal angles θ and ϕ, we compute the properties at a series of values of ϕ at a fixed polar angle of $\theta = 20^\circ$. Since parity remains a crystal symmetry even for arbitrary (θ, ϕ), the Chern numbers must still vanish individually for the Fermi

sheets surrounding parity-invariant momenta, i.e., sheets 7_1, $(7_6,7_7)$, 8, and 9. The Chern numbers of those sheets thus vanish unambiguously in the limit $\theta \to 0$.

According to Table III, this leaves the four pockets $(10_2,10_3,10_4,10_5)$ as the only ones that may acquire a nonzero Chern number as a result of the breaking of M_z symmetry. We find that the Chern number of any one pocket fluctuates between values of -1, 0, and 1 as ϕ is varied; the Chern numbers of inversion-related pairs of sheets are always opposite, as required by parity; and that the sum of the four is always zero. As discussed above, the nonzero individual values result from remnant WPs from the vaporized nodal rings that are left lying inside the sheet in question. Those Weyl nodes move along the ring paths as a function of ϕ, and at critical angles two nodes of opposite chirality join sheet 9 with a pair of inversion-related pockets in band ten. This concerted touching event leads to a net transfer of Chern number between the two pockets in the pair, mediated by sheet 9 whose Chern number remains at zero. One such touching event between sheets 9 and 10_2, as well as the subsequent annihilation of a pair of remnant WPs inside 10_2, are depicted in the Supplemental Material [68].

C. Anomalous Hall conductivity

The intrinsic AHC of bcc Fe has been calculated from first principles by several authors. In Refs. [57] and [47] two different implementations of the Fermi-sea approach of Sec. IV A were used, while in Ref. [30] a FS calculation was carried out along the lines of Sec. IV C. In all these works the focus was on the total intrinsic AHC (i.e., summed over all bands in the Fermi-sea calculations and over all Fermi sheets in the FS calculation). The resulting AHC values were found to be in excellent agreement with one another and in reasonable agreement with measurements at room temperature.

In this section we provide a breakdown of the intrinsic AHC first into band contributions and then into Fermi-sheet contributions. Even though only the total intrinsic AHC is a well-defined physical observable, such decompositions provide insights into the role played by band degeneracies. It can be readily understood that nodal rings do not contribute to the AHC: They form when $\mathbf{M} \parallel [001]$, in which case the AHC vector $\mathbf{K}$ of Eq. (24) is constrained by symmetry to point along k_z, while instead the Berry flux carried by the nodal rings is directed along the tangential direction on the (k_x,k_y) plane. As for the chiral Weyl nodes, they do contribute to the AHC by acting as sources and sinks of Berry curvature, as becomes apparent in the ensuing discussion.

1. Band-by-band decomposition

We work with the AHC vector $\mathbf{K} = \sum_n \mathbf{K}_n$, where the contribution from a single band is given by Eq. (25). Following Ref. [30] we calculate $\mathbf{K}_n$ in reduced coordinates as an average over BZ slices of the Berry flux through the occupied portions of each slice,

$$\mathcal{K}_{nj} = \frac{1}{2\pi}\mathbf{a}_j \cdot \mathbf{K}_n = \frac{1}{n_{\text{slice}}} \sum_{i=1}^{n_{\text{slice}}} \frac{\phi_{nj}(i)}{2\pi}, \tag{49}$$

where the Berry flux $\phi_{nj}(i)$ [Eq. (38)] is evaluated by adding up the Berry phases around small plaquettes covering the occupied portions of the BZ slice (see Sec. V B). Since we take the magnetization to point along $\mathbf{a}_3 = (0,0,a)$, the only nonzero components of the AHC tensor are $\sigma_{xy} = -\sigma_{yx}$, and $\mathcal{K}_{nj}$ only needs to be evaluated for $j = 3$.

The calculated fluxes ϕ_{n3} are piecewise continuous functions of k_z, jumping by integer multiples of 2π when passing through chiral PNs. In our calculations we initially divide the BZ into 800 evenly spaced slices, and whenever $|\phi_{n3}(i+1) - \phi_{n3}(i)| > \pi$ we interpose four additional slices. This allows us to locate more precisely the step discontinuities and to distinguish them from rapid but continuous variations in the flux.

Table IV shows the breakdown of the AHC into band contributions. In the middle columns the dimensionless band contribution given by Eq. (49) is further decomposed according to Eq. (27),

$$\mathcal{K}_{n3} = \mathcal{K}^{(\Omega)}_{n3} + \mathcal{K}^{(\chi)}_{n3}, \tag{50}$$

and in the last column the total contribution from band n is converted to S/cm using $\sigma_{n,xy} = -(e^2/ha)\mathcal{K}_{n3}$. In practice we calculate $\mathcal{K}_{n3}$ and $\mathcal{K}^{(\chi)}_{n3}$ from Eqs. (49) and (29), respectively, and then obtain $\mathcal{K}^{(\Omega)}_{n3}$ as the difference. Recall from Sec. IV B that depending on the placement of the cell boundaries relative to the PNs, integer amounts may get transferred between the two terms in Eq. (50); the values in Table IV are for a BZ cell located between $k_z = -\pi/a$ and $k_z = \pi/a$.

All nonempty bands ($n \leqslant 10$) contribute to the AHC in Table IV, as expected for a Fermi-sea formulation. For bands that are fully occupied ($n \leqslant 4$) the Ω term in Eq. (50) becomes the slice Chern number of Eq. (5) evaluated on the cell boundary at $k_z = \pm\pi/a$; the total $\mathcal{K}_{n3}$ of each of those four bands is not quantized, however, because of the additional term in Eq. (50) contributed by the chiral degeneracies [69]. Since those χ terms sum up to zero over all bands, we can choose to focus exclusively on the Ω terms, in which case the nonquantized part of the AHC is apportioned entirely to the bands crossing E_F ($5 \leqslant n \leqslant 10$). This viewpoint is adopted in the next section.

TABLE IV. Band-by-band decomposition of the AHC of bcc Fe. In the three middle columns the dimensionless AHC is further decomposed according to Eq. (50).

Band n	$\mathcal{K}^{(\Omega)}_{n3}$	$\mathcal{K}^{(\chi)}_{n3}$	$\mathcal{K}_{n3}$	AHC (S/cm)
1	2	0.51	2.51	−3394
2	−6	3.03	−2.97	4018
3	2	1.96	3.96	−5345
4	6	−8.85	−2.85	3840
5	−8.01	6.22	−1.79	2413
6	−7.80	3.27	−4.53	6111
7	14.12	−6.44	7.68	−10 368
8	−3.17	−0.31	−3.48	4702
9	−0.53	1.33	0.80	−1076
10	0.83	−0.72	0.11	−146
Total	−0.56	0	−0.56	755

2. *Fermi-surface decomposition*

Following Sec. IV C, we write the AHC contribution from each Fermi-sheet as an average over BZ slices of Fermi-loop Berry phases [Eq. (44)]. Instead of evaluating the Berry phases $\varphi_{naj}(i)$ directly on the FS as done in Ref. [30], we first compute Berry fluxes and then remove the discontinuities, as explained below. In the case of bands nine and ten with electronlike pockets, we determine the flux $\phi_{nj}(i)$ through the occupied portions of each BZ slice in the same way as in Sec. VI C 1, by adding up the Berry phases around small occupied plaquettes [70]. In the calculations of Sec. VI B 2 we had identified the connected BZ subvolumes where band n is occupied. Since in bcc Fe each subvolume is bounded by a single Fermi sheet S_{na} (this is not true in general), that information can be used to decompose the Berry flux as $\phi_{nj}(i) = \sum_a \phi_{naj}(i)$ by assigning each plaquette to the appropriate subvolume. Having done this for every slice we then set $\varphi_{naj}(i) = \phi_{naj}(i) + 2\pi N_{naj}(i)$, choosing nonzero integers $N_{naj}(i)$ at the critical slices so as to cancel the jumps in $\phi_{naj}(i)$. The procedure is the same for the holelike sheets in bands five to eight, except that we switch from occupied to empty subvolumes and flip the signs of the Berry fluxes. As in Sec. VI C 1, calculations only need to be carried out for $j = 3$.

The Fermi-sheet contributions to the AHC are listed in Table V. Because these are nonquantized contributions, they are only defined modulo $e^2/ha = 1350$ S/cm. This ambiguity arises from the freedom to choose the branch cut of the Berry phase φ_{na3} on some reference slice (Sec. IV C), and below we describe the choices we have made in order to arrive at the values in the table.

For the sheets in groups I, III, IV, V, VI, VII(a), VIII(a), and VIII(b), all of which have zero Chern numbers, we arbitrarily set $\varphi_{na3} = 0$ on an "empty" slice below the Fermi sheet. As an example, Fig. 15(a) shows the evolution of the phase $-\varphi_{na3}$ for $n = 10$ and $a = 1$ [the large pocket centered at Γ in Fig. 10(f)].

TABLE V. Decomposition of the AHC of bcc Fe into nonquantized Fermi-sheet contributions. Symmetry-related sheets are grouped in the same row, and they contribute equal amounts. The two pockets $(10_6, 10_7)$ [group VII(b)] with opposite Chern numbers are treated as a single "composite sheet" and assigned a joint AHC contribution. The shortest distance from each Fermi sheet to a chiral PN on the same band is also indicated.

Band n	Sheet a	Group label	Distance to a PN $(2\pi/a)$	AHC (S/cm)	
5	1	IV	0.30	9	
6	1	III	0.02	–274	
7	1	V	0.06	459	
7	2,3,4,5	VIII(a)	0.01	–203	×4
7	6,7	VIII(b)	0.09	100	×2
8	1	II	0.03	242	
9	1	I	0.02	714	
10	1	VI	0.10	58	
10	2,3,4,5	VII(a)	0.31	–1	×4
10	6,7	VII(b)	0.01	167	
Total				759	

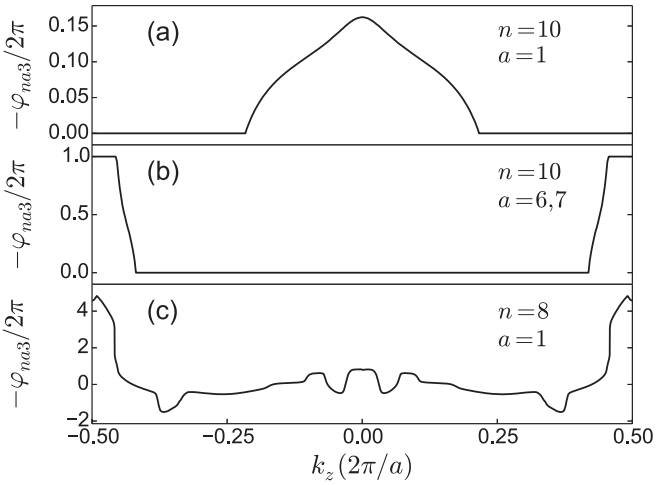

FIG. 15. Evolution with k_z of the Berry phase along the intersection loops between a Fermi sheet and a BZ slice, enforcing continuity from one slice to the next. (a) Fermi pocket 10_1. (b) Topological pockets $(10_6, 10_7)$, treated as a composite Fermi sheet. (c) Fermi sheet 8_1.

Upon hitting the pocket it first rises continuously from zero, reaches a maximum, and then starts to decrease, returning to zero at the top of the pocket.

The two pockets $(10_6, 10_7)$ have nonzero Chern numbers. It is therefore not possible to set the Berry phase to zero both at the bottom and at the top of each of them, while at the same time insisting on a continuous evolution across each pocket [29]. Following Sec. IV C we treat the two pockets as a composite Fermi sheet with an overall zero Chern number and assign them a joint AHC contribution. There are two possibilities for setting $\varphi_{na3} = 0$ on empty slices between the two pockets: either in the wide region around $k_z = 0$, or in the narrow region around $k_z = \pi/a$. We have arbitrarily chosen the former, and the resulting Berry-phase curve is shown in Fig. 15(b) (with the latter choice the entire curve would be shifted downwards by one). The phase $-\varphi_{na3}(k_z)$ rises quickly from zero to 2π while traversing the small pocket with $C = +1$ on the right side of the panel, stays constant at 2π in the narrow region between the two pockets, and finally drops rapidly back to zero while traversing the periodic image of the pocket with $C = -1$ on the left side.

The third case we have encountered is that of the tubular Fermi sheet in band eight. As in the first case considered above the Chern number vanishes, but here there are no empty slices that can be used to set the Berry phase to zero [see Fig. 10(d)]. Instead, we have made in Fig. 15(c) the unique branch choice leading to the correct total intrinsic AHC when summing the contributions from all the Fermi sheets. (We have verified that the curve $-\varphi_3(k_z)$ obtained by summing $-\varphi_{na3}(k_z)$ over all Fermi sheets agrees with Fig. 5 of Ref. [30].) Note the very steep variation in the Berry phase around $k_z = 0.465 \times 2\pi/a$: It is caused by the tiny avoided crossing between sheets (8,9) in Fig. 12 that was mentioned at the end of Sec. VI B 1.

Regarding the magnitude of the nonquantized AHC contributions, inspection of Table V and Fig. 10 reveals that the most significant contributions tend to come from large Fermi sheets with chiral PNs close by. This makes intuitive

sense, as can be seen by considering a typical Fermi pocket with zero Chern number and that can be completely enclosed inside a BZ cell. Using Haldane's formulation with such a choice of BZ cell, its AHC contribution equals the dipole moment of the surface-normal Berry curvature [the term $\mathbf{K}_{na}^{(\Omega)}$ in Eq. (39)]. This quantity scales with the pocket size and is enhanced by the presence of nearby sources and sinks of Berry curvature. As a specific example, compare the pockets $(7_2,7_3,7_4,7_5)$ in group VIII(a) with the pockets $(7_6,7_7)$ in group VIII(b). Although they are almost identical in size and shape, the former contribute twice as much AHC per pocket, by virtue of being much closer to chiral PNs.

The joint AHC contribution from the topological pockets $(10_6,10_7)$ is considerable (about 20% of the total), despite the fact that the pockets themselves are rather small. In this case the AHC contribution scales not with the size of the pockets but with the distance between them, as can be seen from Fig. 15(b). An estimate is provided by the k-space dipole moment between the mirror-symmetric WPs enclosed by each of the two pockets,

$$(+1)\times 0.428+(-1)\times(-0.428)-1=-0.144,$$

in units of $2\pi/a$ (note that the WP at $k_z=0.428\times 2\pi/a$ in Table II acts as a sink of Berry curvature in band nine, and therefore it acts as a source in band ten). This corresponds to a nonquantized AHC contribution of $-0.144\times(-e^2/ha)=194$ S/cm, close to the *ab initio* value of 167 S/cm in Table V; the small overestimation has to do with the finite size of the pockets.

We conclude by analyzing the evolution of the Fermi-sheet Chern numbers and AHC upon varying the Fermi level. Inspection of Fig. 13(a) and Table II shows that at the critical value $\Delta E_F=0.07$ eV the Fermi level coincides with the energy of a double-Weyl node between bands nine and ten, located along the fourfold axis Δ at $k_z=0.48\times 2\pi/a$. The evolution with ΔE_F of sheets 9 and 10_7 is depicted in the Supplemental Material [68]. At the critical value the two sheets touch at the node, and there is a simultaneous touching between sheets 9 and 10_6 at the mirror symmetric node in the lower half of the BZ. Since the chiral charges at the touching points are ± 2, sheet 9 donates to 10_7 a Chern number of $+2$, and it simultaneously receives a compensating amount from 10_6. The net result is that the Chern numbers on pockets 10_6 and 10_7 flip sign, while that of sheet 9 remains at zero. As for the AHC, the joint contribution from the pair $(10_6,10_7)$ changes abruptly by a nonquantized amount, but the total AHC remains continuous because of a compensating discontinuity in the contribution from sheet 9 [71]. This example suggests that a measurement of the AHC cannot by itself resolve the Berry topology of the Fermi sheets.

VII. SUMMARY

In summary, we have used first-principles methods to survey the degeneracies in the spinor band structure of bcc Fe and to calculate the chiral charges of those degeneracies. From the census of chiral band touchings we then determined the Chern numbers of the individual Fermi sheets, paying attention to the subtleties that arise when Fermi sheets are not isolated, but glued together along nodal rings. We found that when the magnetization points along the easy axis [001] most Fermi sheets in bcc Fe are topologically trivial, except for two low-symmetry electron pockets along Δ with Chern numbers ± 1 and four others along Δ' with ill-defined Chern numbers due to Fermi gluing.

The systematic relations we derived between the Fermi-sheet Chern numbers and the enclosed chiral charges are generally applicable to any metal with broken PT symmetry. In particular, we have considered in our formal discussion the case of complex FSs with nested sheet structures, as well as the case where sheets with a Luttinger anomaly are present. Combined with the efficient steepest-descent strategy that was used to locate band degeneracies, our algorithm for determining the FS Chern numbers could be useful in high-throughput *ab initio* searches for topological metals.

The role played by chiral degeneracies in the intrinsic AHC was carefully examined, confirming that they do not pose an impediment to a bulk FS formulation for the nonquantized part. We identified two different ways of decomposing the AHC (band by band and in terms of Fermi sheets) and showed how the two decompositions are related by dipole moments of the distribution inside the BZ of chiral band touchings below the Fermi level. We carried out both decompositions numerically for bcc Fe and found the FS decomposition to be particularly informative and physically transparent: Chiral degeneracies act as sources and sinks of Berry curvature in k space, and the distribution of Berry curvature across the Fermi sheets in turn governs the nonquantized AHC response. So, for example, Fermi sheets with chiral PNs very nearby tend to contribute more to the AHC than otherwise similar Fermi sheets that are farther from chiral PNs.

By showing that 2 of 18 Fermi sheets in bcc Fe are topologically nontrivial, we have established that nonzero Chern numbers are not only possible, in principle, in T-broken FSs, but that they actually occur in realistic ferromagnetic band structures. Further studies on other ferromagnets will be needed before it becomes clear how common they are. Since symmetry was seen to play an important role, it would be interesting to explore materials with other symmetries, e.g., a sixfold axis. The fact that parity imposes zero Chern numbers on most Fermi sheets in bcc Fe suggests that topologically nontrivial sheets may be more common in P-broken metals. Known examples include MnSi and related ferromagnetic compounds with the B20 structure and also metals such as $LiOsO_3$ that undergo ferroelectriclike polar distortions [72].

By varying either the magnetization direction or the Fermi level, we were able to change the Chern numbers on the FS of bcc Fe. The process consisted of concerted chiral touching events involving three electronlike Fermi sheets, with a large, topologically trivial sheet in band nine mediating the transfer of Chern number between two small enclosed pockets in band ten. The experimental consequences of such topological transitions remain largely unexplored. The manner in which the topological properties can change as a function of other external parameters such as pressure, e.g., via discrete Fermi-sheet reconnection or PN pair annihilation or creation events, is also an attractive subject for future investigation.

ACKNOWLEDGMENTS

This work was supported by Grants No. MAT2012-33720 from the Ministerio de Economía y Competitividad (Spain), No. CIG-303602 from the European Commission, by NSF Grant No. DMR-14-08838, and by a grant from the Simons Foundation (No. 305025 to D. Vanderbilt).

APPENDIX: SYMMETRY CONSTRAINTS

In this appendix we list the constraints imposed on several k-space quantities by the spatial inversion symmetry P of bcc Fe and also by the additional mirror symmetry M_z that is present when the magnetization points along the easy axis [001]. The quantities of interest are the energy eigenvalues $E_n(\mathbf{k})$, the Berry curvature $\mathbf{\Omega}_n(\mathbf{k})$, the chiral charge $\chi_{n\alpha}$, and the slice Chern numbers $C_n(k_z)$ and $\widetilde{C}_n(k_z)$.

Inversion symmetry implies

$$E_n(-\mathbf{k}) = E_n(\mathbf{k}), \tag{A1}$$

$$\mathbf{\Omega}_n(-\mathbf{k}) = \mathbf{\Omega}_n(\mathbf{k}), \tag{A2}$$

$$\chi_{n\alpha'} = -\chi_{n\alpha}, \tag{A3}$$

where Eq. (A3) follows from Eqs. (10) and (A2), and the node $n\alpha'$ in Eq. (A3) is the parity-reflected partner of $n\alpha$. Evaluating Eq. (5) at $-k_z$ we find

$$C_n(-k_z) = \frac{1}{2\pi}\int d^2k\, \Omega_{n,z}(-\mathbf{k}) = C_n(k_z), \tag{A4}$$

where we first made the change of variables $k_x \to -k_x$, $k_y \to -k_y$, and then used Eq. (A2). Because of the periodicity condition (6) we also have

$$C_n(\pi/a - k_z) = C_n(\pi/a + k_z), \tag{A5}$$

so that $C_n(k_z)$ is even with respect to both $k_z = 0$ and $k_z = \pi/a$, and the same is, of course, true for $\widetilde{C}_n(k_z)$.

The presence of mirror symmetry M_z implies

$$E_n(M_z\mathbf{k}) = E_n(\mathbf{k}), \tag{A6}$$

$$\Omega_{n,x}(M_z\mathbf{k}) = -\Omega_{n,x}(\mathbf{k}), \tag{A7}$$

$$\Omega_{n,y}(M_z\mathbf{k}) = -\Omega_{n,y}(\mathbf{k}), \tag{A8}$$

$$\Omega_{n,z}(M_z\mathbf{k}) = \Omega_{n,z}(\mathbf{k}), \tag{A9}$$

$$\chi_{n\alpha'} = -\chi_{n\alpha}, \tag{A10}$$

where $M_z(k_x,k_y,k_z) = (k_x,k_y,-k_z)$ and $n\alpha'$ is the mirror-reflected partner of $n\alpha$.

[1] S. Murakami, New J. Phys. **9**, 356 (2007).
[2] X. Wan, A. M. Turner, A. Vishwanath, and S. Y. Savrasov, Phys. Rev. B **83**, 205101 (2011).
[3] A. A. Burkov and L. Balents, Phys. Rev. Lett. **107**, 127205 (2011).
[4] K.-Y. Yang, Y.-M. Lu, and Y. Ran, Phys. Rev. B **84**, 075129 (2011).
[5] A. M. Turner and A. Vishwanath, in *Topological Insulators* (Elsevier, Amsterdam, 2013), Chap. 11, p. 293.
[6] F. D. M. Haldane, arXiv:1401.0529.
[7] S.-M. Huang, S.-Y. Xu, I. Belopolski, C.-C. Lee, G. Chang, B. Wang, N. Alidoust, G. Bian, M. Neupane, C. Zhang, S. Jia, A. Bansil, H. Lin, and M. Z. Hasan, Nat. Commun. **6**, 7373 (2015).
[8] H. Weng, C. Fang, Z. Fang, B. A. Bernevig, and X. Dai, Phys. Rev. X **5**, 011029 (2015).
[9] S.-Y. Xu, I. Belopolski, N. Alidoust, M. Neupane, G. Bian, C. Zhang, R. Sankar, G. Chang, Z. Yuan, C.-C. Lee, S.-M. Huang, H. Zheng, J. Ma, D. S. Sanchez, B. Wang, A. Bansil, F. Chou, P. P. Shibayev, H. Lin, S. Jia, and M. Z. Hasan, Science **349**, 613 (2015).
[10] B. Q. Lv, H. M. Weng, B. B. Fu, X. P. Wang, H. Miao, J. Ma, P. Richard, X. C. Huang, L. X. Zhao, G. F. Chen, Z. Fang, X. Dai, T. Qian, and H. Ding, Phys. Rev. X **5**, 031013 (2015).
[11] S.-Y. Xu, N. Alidoust, I. Belopolski, C. Zhang, G. Bian, T.-R. Chang, H. Zheng, V. Strokov, D. S. Sanchez, G. Chang, Z. Yuan, D. Mou, Y. Wu, L. Huang, C.-C. Lee, S.-M. Huang, B. Wang,, A. Bansil, H.-T. Jeng, T. Neupert, A. Kaminski, H. Lin, S. Jia, and M. Z. Hasan, arXiv:1504.01350 [Nat. Phys. (to be published)].
[12] J. Liu and D. Vanderbilt, Phys. Rev. B **90**, 155316 (2014).
[13] Z. K. Liu, B. Zhou, Y. Zhang, Z. J. Wang, H. M. Weng, D. Prabhakaran, S.-K. Mo, Z. X. Shen, Z. Fang, X. Dai, Z. Hussain, and Y. L. Chen, Science **343**, 864 (2014).
[14] M. Neupane, S. Xu, R. Sankar, N. Alidoust, G. Bian, C. Liu, I. Belopolski, T.-R. Chang, H.-T. Jeng, H. Lin, A. Bansil, F. Chou, and M. Z. Hasan, Nat. Commun. **5**, 3786 (2014).
[15] M. V. Berry, Proc. R. Soc. London, Ser. A **392**, 45 (1984).
[16] C. Fang, M. J. Gilbert, X. Dai, and B. A. Bernevig, Phys. Rev. Lett. **108**, 266802 (2012).
[17] S. Murakami and S.-i. Kuga, Phys. Rev. B **78**, 165313 (2008).
[18] L. M. Falikov and J. Ruvalds, Phys. Rev. **172**, 498 (1968).
[19] A. P. Cracknell, J. Phys. C: Solid State Phys. **2**, 1425 (1969).
[20] A. P. Cracknell, Phys. Rev. B **1**, 1261 (1970).
[21] F. D. M. Haldane, Phys. Rev. Lett. **93**, 206602 (2004).
[22] X.-L. Qi, T. L. Hughes, and S.-C. Zhang, Phys. Rev. B **81**, 134508 (2010).
[23] P. Hosur, X. Dai, Z. Fang, and X.-L. Qi, Phys. Rev. B **90**, 045130 (2014).
[24] J.-H. Zhou, J. Hua, Q. Niu, and J.-R. Shi, Chin. Phys. Lett. **30**, 027101 (2013).
[25] L. Lu, L. Fu, J. D. Joannopoulos, and M. Soljačić, Nat. Photonics **7**, 294 (2013).
[26] Y. Chen, D. L. Bergman, and A. A. Burkov, Phys. Rev. B **88**, 125110 (2013).
[27] M. Hirayama, R. Okugawa, S. Ishibashi, S. Murakami, and T. Miyake, Phys. Rev. Lett. **114**, 206401 (2015).
[28] S.-M. Huang, S.-Y. Xu, I. Belopolski, C.-C. Lee, G. Chang, B. Wang, N. Alidoust, M. Neupane, H. Zheng, D. Sanchez, A. Bansil, G. Bian, H. Lin, and M. Z. Hasan, arXiv:1503.05868.
[29] D. Vanderbilt, I. Souza, and F. D. M. Haldane, Phys. Rev. B **89**, 117101 (2014).
[30] X. Wang, D. Vanderbilt, J. R. Yates, and I. Souza, Phys. Rev. B **76**, 195109 (2007).
[31] F. R. Klinkhamer and G. E. Volovik, Int. J. Mod. Phys. A **20**, 2795 (2005).

[32] G. E. Volovik, Lect. Notes Phys. **718**, 31 (2007).

[33] A. V. Gold, J. Low Temp. Phys. **16**, 3 (1974).

[34] M. Singh, C. S. Wang, and J. Callaway, Phys. Rev. B **11**, 287 (1975).

[35] G. G. Lonzarich, in *Electrons in Metals*, edited by M. Springfield (Cambridge University Press, Cambridge, UK, 1980), p. 225.

[36] M. Kohmoto, B. I. Halperin, and Y.-S. Wu, Phys. Rev. B **45**, 13488 (1992).

[37] Although a 2π ambiguity is inherent to the definition of the Berry phase, its presence in Eq. (9) may seem puzzling from the point of view of Stokes' theorem. Note, however, that Stokes' theorem cannot be applied globally to a BZ slice with nonzero Chern number using a periodic gauge, as it is not possible to extend a smooth gauge choice from the boundary into the interior: There will always be vortexlike singularities left at isolated points, which provide additional $\pm 2\pi$ contributions [38,39]. Gauge discontinuities (pairs of vortices and antivortices) can, in fact, be generated even when the slice Chern number vanishes.

[38] M. Kohmoto, Ann. Phys. (N.Y.) **160**, 343 (1985).

[39] Y. Hatsugai, Phys. Rev. Lett. **71**, 3697 (1993).

[40] A. A. Burkov, M. D. Hook, and L. Balents, Phys. Rev. B **84**, 235126 (2011).

[41] Y. Kim, B. J. Wieder, C. L. Kane, and A. M. Rappe, Phys. Rev. Lett. **115**, 036806 (2015).

[42] D. Xiao, M.-C. Chang, and Q. Niu, Rev. Mod. Phys. **82**, 1959 (2010).

[43] N. Nagaosa, J. Sinova, S. Onoda, A. H. MacDonald, and N. P. Ong, Rev. Mod. Phys. **82**, 1539 (2010).

[44] Equation (27) is analogous to a formal real-space expression in Ref. [45] for the electric polarization of an insulating crystal (more precisely, it is an expression for the first-order change in polarization under a perturbation).

[45] R. M. Martin, Phys. Rev. B **9**, 1998 (1974).

[46] This is also true when the sum runs over an isolated subset of bands, i.e., a set of adjacent bands that can have PN degeneracies among themselves, but which remain separated from lower or higher bands by finite gaps everywhere in the BZ.

[47] X. Wang, J. R. Yates, I. Souza, and D. Vanderbilt, Phys. Rev. B **74**, 195118 (2006).

[48] P. Giannozzi *et al.*, J. Phys. Condens. Matter **21**, 395502 (2009).

[49] J. P. Perdew, K. Burke, and M. Ernzerhof, Phys. Rev. Lett. **77**, 3865 (1996).

[50] N. Marzari and D. Vanderbilt, Phys. Rev. B **56**, 12847 (1997).

[51] I. Souza, N. Marzari, and D. Vanderbilt, Phys. Rev. B **65**, 035109 (2001).

[52] A. A. Mostofi, J. R. Yates, Y.-S. Lee, I. Souza, D. Vanderbilt, and N. Marzari, Comput. Phys. Commun. **178**, 685 (2008).

[53] T. Fukui, Y. Hatsugai, and H. Suzuki, J. Phys. Soc. Jpn. **74**, 1674 (2005).

[54] R. D. King-Smith and D. Vanderbilt, Phys. Rev. B **47**, 1651 (1993).

[55] This algorithm may fail if, for example, a double-Weyl node lies very close to a plaquette. The Berry flux through the plaquette can then be of the order of 2π, which would be mistaken for a flux close to zero. This ambiguity can be avoided by evaluating the flux directly from the gauge-invariant Berry curvature.

[56] H. Yamagami, J. Phys. Soc. Jpn. **67**, 3176 (1998).

[57] Y. Yao, L. Kleinman, A. H. MacDonald, J. Sinova, T. Jungwirth, D.-S. Wang, E. Wang, and Q. Niu, Phys. Rev. Lett. **92**, 037204 (2004).

[58] V. Heine, *Group Theory in Quantum Mechanics* (Pergamon, New York, 1960).

[59] Note that the projected BZ at the bottom of Fig. 3 has twice the area of the (001) surface BZ of the bcc lattice and that the symmetry labels $\overline{\mathrm{M}}$ and $\overline{\mathrm{X}}$ denote different points in each case: $\overline{\mathrm{X}}$ in the projected BZ corresponds to $\overline{\mathrm{M}}$ in the surface BZ, and $\overline{\mathrm{M}}$ in the projected BZ is a periodic image of $\overline{\Gamma}$ in the surface BZ. Thus, the fourfold axes that project onto $\overline{\Gamma}$ and $\overline{\mathrm{M}}$ in Fig. 3 are really the same axis, apart from a vertical offset of $2\pi/a$.

[60] The effective Hamiltonian for a pair of crossing bands can only contain σ_1 and σ_3 Pauli matrices; zeroing their coefficients generates a degeneracy. Alternative arguments for the codimension of two for states in a C_2T symmetry plane can be found in Ref. [61].

[61] C. Fang and L. Fu, Phys. Rev. B **91**, 161105 (2015).

[62] Note that the gap function $(E_{n+1,\mathbf{k}} - E_{n\mathbf{k}})^2$ is differentiable everywhere in the BZ, including at degeneracy points where the bands disperse linearly in one or more directions. In our Wannier-based implementation, the needed band gradients are readily available [63] .

[63] J. R. Yates, X. Wang, D. Vanderbilt, and I. Souza, Phys. Rev. B **75**, 195121 (2007).

[64] H. Weng, Y. Liang, Q. Xu, R. Yu, Z. Fang, X. Dai, and Y. Kawazoe, Phys. Rev. B **92**, 045108 (2015).

[65] M. Zeng, C. Fang, G. Chang, Y.-A. Chen, T. Hsieh, A. Bansil, H. Lin, and L. Fu, arXiv:1504.03492.

[66] J. Callaway and C. S. Wang, Phys. Rev. B **16**, 2095 (1977).

[67] The explanation given in Sec. VI A 2 for the formation of nodal rings on mirror planes carries over to the SOC-free bands. The mirror-symmetry eigenvalues are now ± 1, and nodal rings can only form between like-spin bands.

[68] See Supplemental Material at http://link.aps.org/supplemental/10.1103/PhysRevB.92.085138 for a depiction of touching events between Fermi sheets accompanied by a transfer of Chern number.

[69] This can be understood by noting that for a full band the summand in Eq. (49) becomes an integer slice Chern number, whose average is noninteger whenever PN-induced step discontinuities are present.

[70] Contrary to Sec. VI C 1, here we are only interested in the nonquantized part of the flux. For that purpose it is sufficient to apply the plaquette subdivision strategy of Sec. V B to the plaquettes along the edge between occupied and empty regions and not to those that are completely surrounded by other occupied plaquettes.

[71] We do not observe any discernible effect on the AHC as the Fermi level passes through a Weyl node. Rapid variations in $\sigma_{xy}(E_F)$ are not generally associated with Weyl nodes at E_F as stated in Ref. [26], but with avoided crossings.

[72] Y. Shi, Y. Guo, X. Wang, A. J. Princep, D. Khalyavin, P. Manuel, Y. Michiue, A. Sato, K. Tsuda, S. Yu, M. Arai, Y. Shirako, M. Akaogi, N. Wang, K. Yamaura, and A. T. Boothroyd, Nat. Mater. **12**, 1024 (2013).